CHAPTER 15

Solid-state NMR of Organic Electronics

Ryan Nieuwendaal

Materials Science and Engineering Division, National Institute of Standards and Technology, 100 Bureau Drive, Gaithersburg, MD 20899-8541, United States of America

E-mail: ryann@nist.gov

Abstract

Organic materials that exhibit high charge conductivities have potential uses in a number of electronics application areas, such as photovoltaics and flat panel displays and what once was a perpetual “on the horizon” class of materials, organic electronics are finding many real-world uses in a number of flexible electronics applications such as wearable sensors. However, regardless of the applied technology, precise knowledge of the morphologies of the organic molecules that comprise the active material are critical to optimizing the functionality. Solid-state NMR is a powerful analytical tool for deciphering local structures in complex morphologies and measuring molecular dynamics in dynamically heterogeneous materials. In this review, we cover recent solid state NMR works that have focused on organic electronics materials such as polythiophenes, polyphenylene vinylenes, polyfluorenes, and a number of donor-acceptor polymers with applications in organic electronics, namely organic thin film transistors, organic light emitting diodes, and organic photovoltaics.

15.1 Introduction

Since the Nobel Prize was awarded to Alan MacDiramid, Hideki Shirakawa, and Alan Heeger in 2000 "for the discovery and development of conductive polymers" the materials science community has pushed forward in this area in hopes of engineering organic electronic (OE) molecules with desirable charge transport characteristics for commercial uses. Initial target applications focused on photovoltaic (PV) solar panel arrays for commercial, farm, and residential uses, but due to the decreasing price of Si, still underperforming organic photovoltaics (OPVs) vs. Si, and relative instability of organic photovoltaics (OPVs), markets have shifted to flexible electronics and bioelectronics applications due to the application tailorability and mechanical flexibility of the organic counterparts. The OE community has focused on chemistry improvements, increasing scale-up, and improved device design to incorporate high-throughput processing. Organic transistors and photovoltaics have seen tremendous strides in charge mobility and photoconversion efficiency, respectively, but primarily at the lab-level. Much credit goes to the polymer organic chemistry community for synthesizing increasingly complex molecules by design; in the span of almost two decades, the molecules under study have gone from as simple as poly(acetylene) [1] to as complex as polymers with multiple units of alternating benzothiadiazole (BT), diketopyrrolopyrrole (DPP), isoindigo, and/or terthiophene monomer units. [2] These advancements have helped drive the upward trend in reported carrier mobilities for both vacuum deposited organic small molecules (10 – 20 $cm^2 V^{-1} s^{-1}$) [3] and solution-processed polymer films (5 – 10 $cm^2 V^{-1}$ s-1) [4], surpassing amorphous Si (1 – 3 $cm^2 V^{-1} s^{-1}$) [5] but still trailing single crystalline Si (100 – 1500 $cm^2 V^{-1} s^{-1}$). [6,7] Power conversion efficiency values in organic solar cells have trended upward as well, now reaching a maximum power conversion efficiency value of 17 % [8] approaching the best achieved Si solar cell (26 %). [9]

Despite the tremendous progress of the best achieved organic photovoltaic cells and organic transistors, the progress has occurred primarily heuristicly by iterative manipulation of the chemistry

and processing parameters. There have been two primary obstacles to designing organic electronics devices based on morphology. First, although the morphologies of organic electronic films clearly play a role in a number of device metrics such as carrier mobility [10] and optical absorption [11], they have generally been poorly understood, highly process depedent, and highly sample history dependent. For instance, for the semicrystalline polythiophenes there are established correlations between carrier mobility and crystallinity, molar mass, and phase [10,12], but the molecular underpinnings of these correlations have been clouded by uncertainties in the number and role of non-crystalline tie chains [13,14], the differences in intra- and inter-chain charge transport both in and outside of the crystal phases [15], and quantitative metrics of crystallinity. Furthermore, these correlations have not been observed in a number of next-generation polymers that exhibit little appreciable long range order [16], which makes it difficult to come up with "general rules." Second, the complete prediction of an OE device based on the photophysics and a known, understood morphology remains far on the horizon due to unreasonable computation times that would be needed for predicting the electronic structure in such a heterogeneous material. Without predictive capability of the electronic structures, it is impossible to calculate the functionality of such devices.

15.2 Solid-state NMR, organic electronics materials, and structure-property relationships

Solid-state nuclear magnetic resonance (NMR) has a rich history as a characterization tool for commercial polymers such as polyolefins [17,18,19,20], celluloses [21,22,23], and other plastics such as nylons and nylon composites [24,25,26], polyesters [27], and polycarbonates. [28,29,30] In this chapter, we will highlight the use of solid state NMR in the area of organic electronics for determining local structures and molecular dynamics. Unlike conventional polymers, the contributions of solid state NMR relative to other techniques have been hindered primarily for two major reasons. First, unlike traditional polymers, the ≈100 nm thick polymer films used in OE devices at the lab scale are deposited on small

mass scales (≈0.1 mg) for higher throughput vetting of casting (i.e., spin-casting, doctor blading) and post-processing (i.e., thermal or solvent annealing) conditions. These small sample sizes make systematic investigations of structure-property-processing relationships by NMR a challenge. Furthermore, it is not straightforward to scale up sample mass since the morphologies are typically highly dependent on thickness as well as processing. Second, the OE field has seen a continuous and rapid fine tuning of the chemistry of the organic molecules used in OE devices. As a result, uncertainty in processability and physical properties such as miscibility and crystallization have not seemingly been too significant a bottleneck for improving performance at the lab scale. As there is a move towards scaling up, and as there is motivation to translate OE film performance observed on the lab scale to a larger scale, there will likely be a concomitant drive to understand morphology-functionality-processing correlations. However, until that time arrives detailed structure-property-processing correlations are up until this point, quite rare.

This book chapter will primarily be summarizing the work of solid state NMR experiments that are utilized for understanding the unknown morphologies and dynamics of polymer structures for OE devices. These measurements are integrated with complimentary non-NMR characterization methods to (1) connect the NMR data to methods that are either faster, simpler, or could be utilized for fast sampling / in situ observation of morphology evolution (i.e. via roll-to-roll-coating) and (2) develop a deeper understanding than just NMR alone and provide context for NMR interpretation. Furthermore, this book chapter notes when NMR observations have been reproduced in the literature. In the bulk of this work, it is assumed that the influence of unpaired and conductive electrons is negligible and NMR observables such that the Knight shift, paramagnetic shifts, and paramagnetic induced relaxation are undetectable. There are several works in which solid state NMR is utilized to understand the electronic structure. [31, 32, 33, 34, 35, 36, 37] In these cases, for the most part, the nuclear positions are well

understood and the electronic structure is the unknown. In this book chapter, the nuclear positions of the morphologies are thought of as the unknowns.

Solid-state NMR is a powerful method for probing local structure and dynamics in heterogeneous solids, and in many cases, NMR can quantify the degree of and characterize the nature of the heterogeneity, whether it is a semicrystalline polymer, a mesogen with complex phase behavior, or a polymer blend. One of the commercial driving forces for organic transistors and photovoltaics is that they are solution processable so can potentially be manufactured in large volumes at low cost. For polymers that crystalize, the crystal growth kinetics are important in determining the final morphology, and the solubility, solution history, and drying rate are all important factors in determining the final morphology of the solid. [38] For polymer blends, such as those used in organic photovoltaics, the polymer miscibility, co-solubility in the common solvent, and the possibility of co-crystallization are added factors in determining the domain sizes, phase separation, and interfacial structure in the deposited film. [39] NMR is well-suited for probing the phase behavior, local structure and molecular dynamics of all of those cases.

This book chapter will highlight three classes of materials: small molecules for transistors and light emitting diodes (LED), polymers for transistors and light emitting diodes, and polymer blends for organic photovoltaics. The examples are not exhaustive, rather the sampling is intended to be representative of the possibilities of the technique. We have laid these three sections out in terms of increasing complexity of the thermodynamics, possible structures, and materials design rules. Measurements of mesophase behavior, molecular dynamics and molecular orientation will be highlighted for small molecule films. The NMR of neat polymers will generally focus on spectral assignments and phase behavior (i.e. crystallization, paracrystallinity), measurements of molecular dynamics on 10^{-6} s to 1 s time scales, and methods for determining molecular packing structures. Finally, the design rules of polymer blends used for organic photovoltaics are the most complex due to added effects of miscibility,

phase separation of donor and acceptor molecules and the domain sizes therein. Despite the diversity of films under study, NMR is unparalleled in its ability to quantify the distributions of such phases of interest. Successful application of solid state NMR for probing and quantifying local structures and dynamics in heterogeneous polymer solids hinges on sufficient contrast, whether it be relaxation time contrast via differences in molecular dynamics, or chemical shift contrast via differences in chemistry, molecular conformation, or molecular packing.

15.2.1 Disordered small molecules and oligomers for transistors and LEDs

Polyfluorenes (PFs) have been used for applications in organic light emitting diodes (OLEDs), and studies have shown that photoluminescence and electroluminescence photon energies and efficiencies depend on PF backbone order, conjugation length, and alignment. [40] As a result, OLED properties have been tailored via variations in side chain chemistry, end-group chemistry, and film deposition protocols. [41,42] Depending on processing, PF has shown three distinct phases, an amorphous phase and two crystalline phases [15], and oligofluorenes have been used to understand these phases and establish structure-property relationships. [43] In 2012, Bernardinelli and co-workers utilized solid-state NMR, including dipolar chemical shift (DIPSHIFT) [44] and centerband only detection of exchange (CODEX) [45] experiments, to probe the molecular dynamics of a series of oligofluorenes that exhibited distinct phases from X-ray diffraction and differential scanning calorimetry (DSC). [46]

DIPSHIFT measures the reduction (i.e., scaling 0 to 1) of a known ^{1}H-^{13}C dipolar coupling caused by reorientations (μs – ms) of hydrogen-carbon bonds. ^{13}C CODEX measures reorientations of the ^{13}C chemical shift tensor (and thereby ^{13}C-including bonds) on 0.001 – 1 s time scales. As such, Bernardinelli et al utilized the CODEX and DIPSHIFT experiments to probe the main chain and side chain motions, respectively (Figure 15.1). In the absence of molecular motion and T_2 effects the DIPSHIFT curve, in which the x-axis spans from 0 to one rotor period (t_r), will be “U-shaped” with $S(t_1=0)/S_0 = 1$, $S(t_1=t_r/2)/S_0$

= 0, and $S(t_1=t_r)/S_0 = 1$, where t_1 is the dephasing time, $S(t_1)$ is the NMR signal as a function of t_1, and S_0 is the signal at $t_1 = 0$. As C-H bond reorientations become more higly dynamic (increased amplitude of motion) on 10^{-6} s to 10^{-3} s time scales, S/S_0 values at $t_1 = t_r/2$ should increase depending on the geometry of the motion, approaching one as the motion becomes isotropic. As shown in Figure 15.1 (a)-(c), all three oligomers exhibited monotonic changes in their DIPSHIFT curves with increasing temperature indicative of changes in the methylene bond rotational dynamics. At the glass transition temperature (T_g) + 29°C the trimer displayed essentially isotropic motion, as observed from the high $S(t_1=t_r/2)/S_0$ value; the pentamers and heptamers displayed anisotropic motions at T_g + 29 °C.

As shown from the CODEX results (Figure 15.1d-g), the trimers are unique in that essentially all the molecules exhibit high angle (isotropic) reorientations in the molecular backbone (carbons 5 and 7, Figure 15.1d). The pentamers exhibited a bimodal distribution of large and small reorientation angles, which were assigned to backbone motions in the non-crystalline and crystalline phases at 303 K, respectively, and upon annealing these backbone motions were suppressed (Figure 15.1e). The septamer exhibits high reorientation angles at 333 K, which are invariant to annealing (Figure 15.1f). These motions were ascribed to its helical structure, and in order to precisely determine structure the authors performed density functional theory (DFT) calculations of geometry-optimized structures of the oligofluorenes in vacuum. ^{13}C chemical shifts were predicted and compared to experimental ^{13}C cross-polarization magic angle spinning (CPMAS) [47] spectra, and the calculated electron absorption spectrum was compared to experiment. Even in the absence of intermolecular interactions, multiple local minima were observed for the different molecular configurations, but based on the agreements of the calculated chemical shifts with experiment, a selected few molecular conformations were identified as possible candidate structures. The influence of molecular packing on the chain structure, which was ignored in this study, can be explored with nuclear independent chemical shift (NICS) as discussed below. [48]

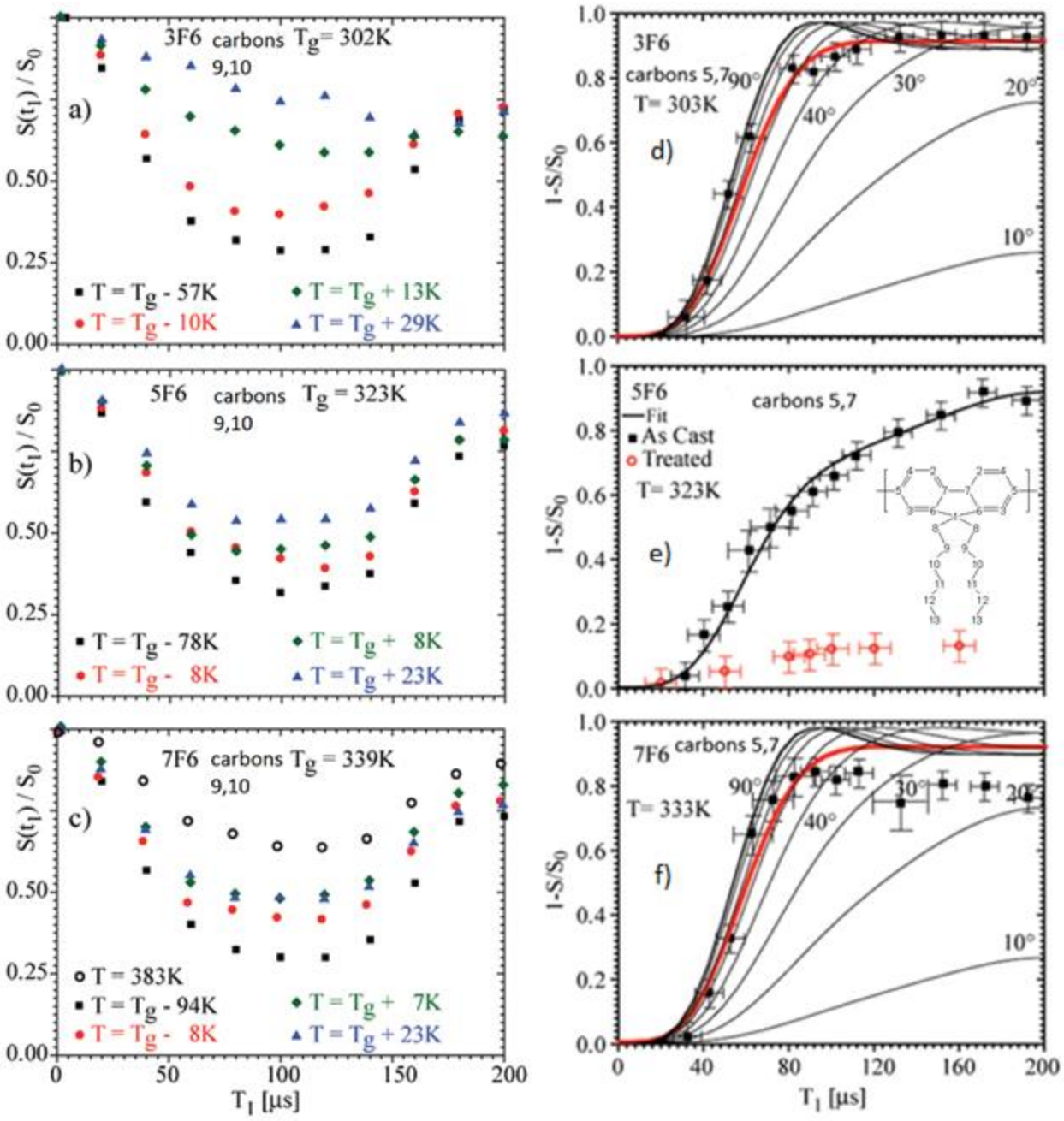

Figure 15.1: (a)-(c) ^{13}C-^{1}H DIPSHIFT patterns for the interior side chain methylene carbons (9,10) of tri- (a), penta- (b), and septa-fluorene (c). (d) – (f) ^{13}C CODEX curves as a function of the dephasing time (T_1) for tri- (d), penta- (e), and septa-fluorene (f). The chemical structure is given as an inset in (e). Adapted with permission from Ref [46]. Copyright 2012 American Chemical Society.

Thin amorphous layers of small organic molecules have been used for electron transport layers in OLED devices. One important property for controlling the mobilities of these layers is the net (residual) molecular orientation distribution, which depends heavily on the method of film deposition. Hence, in order to establish clear structure-property-processing relationships, a quantitative metric of the molecular orientation distribution is needed. In 2017, Suzuki et al. utilized static ^{31}P NMR and chemical shift anisotropy (CSA) analysis to calculate the P=O bond orientation distribution relative to the substrate for both a vacuum-deposited and drop-cast phenyldi(pyren-1-yl) phosphine oxide ($POPy_2$) film. [49] Dynamic nuclear polarization was used for signal enhancement ($\varepsilon = 6.0$) due to the low masses of the thin films (1.5 and 2.8 μm thick) on silicon substrates (30 μm). Based on fits of the CSA patterns (Figure 15.2b-c), it was shown that the drop-cast films exhibited isotropic distributions of P=O bonds (Figure 15.2e), whereas the vacuum deposited film exhibited a preference for P=O bonds oriented normal to the substrate plane by a factor of 2 (Figure 15.2d).

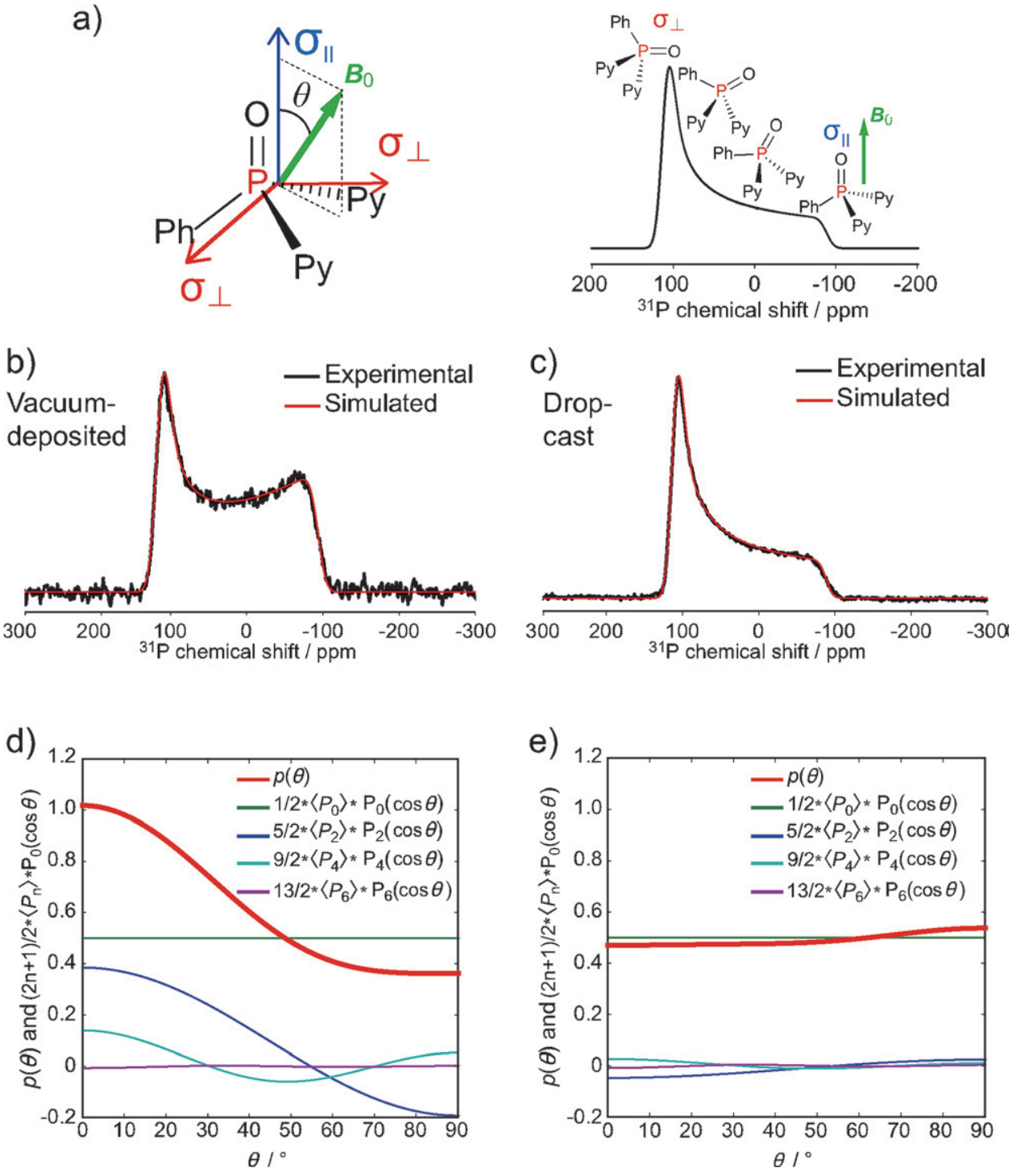

Figure 15.2: (a) Schematic of the ^{31}P chemical shift tensor in the molecular axis frame of $POPy_2$ (left), and the simulated ^{31}P CSA pattern with corresponding molecular orientations with respect to B_0 (right). (b)-(c) Static ^{31}P NMR lineshapes for vacuum-deposited (b) and drop-cast (c) POPy2. (d)-(e) Orientation

distributions of vacuum-deposited (d) and drop-cast (e) $POPy_2$. Adapted with permission from Ref [49]. Copyright 2017 John Wiley and Sons.

15.2.2 Polymers for transistors and LEDs

Poly(p-phenylene vinylene) (PPV)s comprise another class of polymers that have been used for OLEDs. Studies have shown that side chain molecular structure and OLED film processing effect electroluminescence quantum efficiency and photon energy by controlling the main chain conformational defect density. [50,51] In order to establish how these defects arise, quantitative metrics of molecular structure and dynamics are needed. In their 2003 article, deAzevedo and coworkers reported results of ^{13}C CODEX experiments of chain motions in poly(p-phenylene vinylene) (PPV) [52]. Carbon sites on the PPV main chain undergo ^{13}C chemical shift exchange due to 180^o phenylene ring flips (Figure 15.3a) that induce motional narrowing and coalescence of the protonated ^{13}C resonances (see sites 2-3, 5-8 in Figure 15.3a) upon heating (Figure 15.3b). To distinguish between the fractions of segments that undergo these 180^o flips from those that simply undergo low angle reorientations with no flip, the authors introduced a CODEX variant, non-recoupled (NR-) CODEX and compared CODEX curves of the non-protonated carbons (Figure 15.3c), which are not sensitive to phenylene flips, to those of the protonated carbons (Figure 15.3d), which are. Fits were performed on both curves including both low-angle reorientations as well as ring flips (Figure 15.3e-f). Of the segments undergoing main chain reorientations (> 30 %), the fraction of segments found undergoing imprecise ring flips (of angle 30^o) was 0.69 and the fraction of segments undergoing low angle (9^o) reorientations was 0.31. By performing CODEX experiments as a function of temperature, it was found that the activation energy of the phenylene ring flips was determined to be 23 ± 3 kJ/mol.

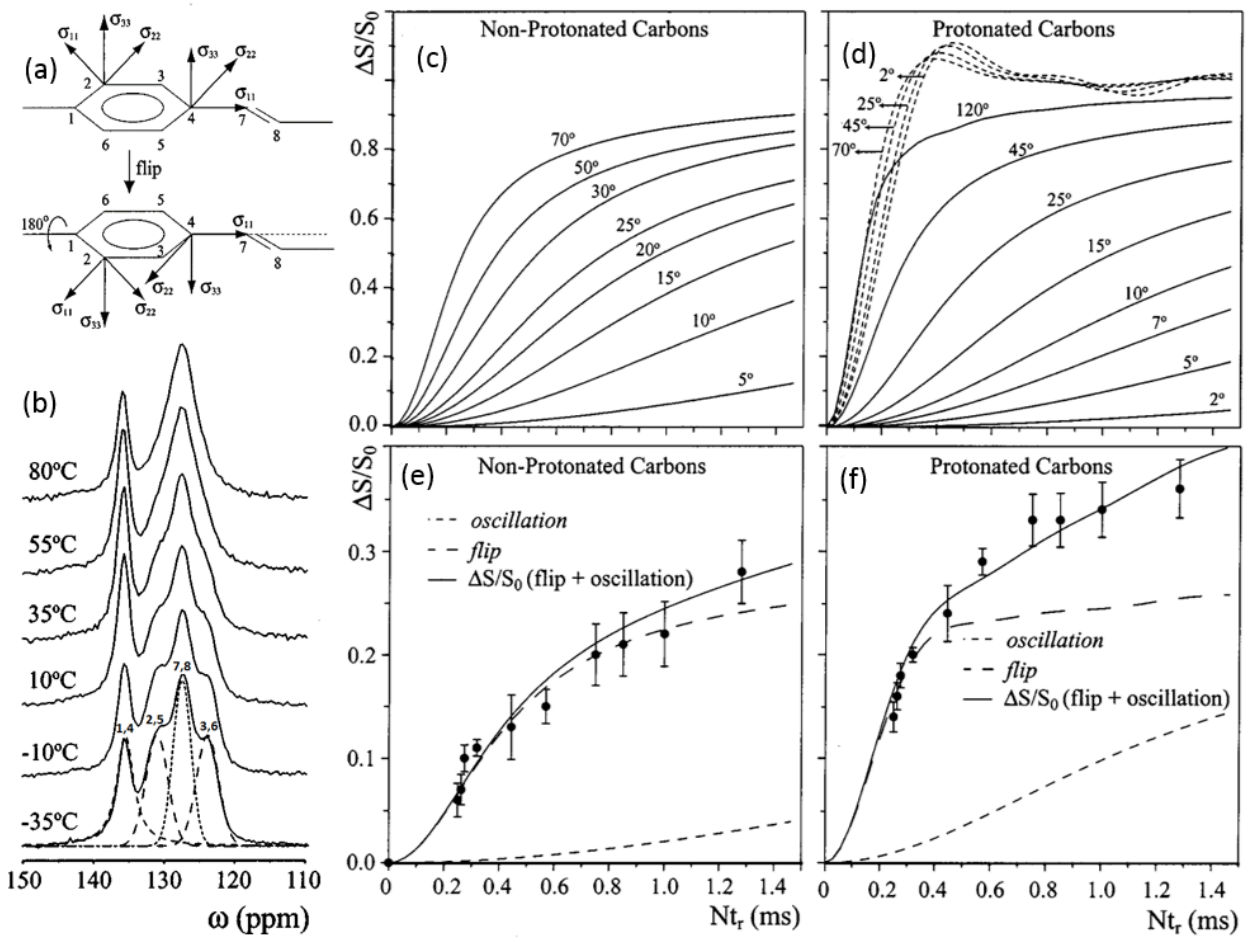

Figure 15.3: (a) Schematic of the PPV monomer unit depicting the chemical shift tensor components (σ_{11}, σ_{22}, σ_{33}) and their change in orientation after a ring flip. (b) Solid-state ^{13}C NMR spectra of PPV as a function of temperature. The numbers denote the assignment in (a). (c)-(d) Simulated CODEX curves for the non-protonated (c) and protonated (d) ^{13}C of PPV for different oscillation angles. Solid lines correspond to simulations for small angle oscillations (θ) or an odd number of imprecise ring flips (θ + 180°) and dashed lines correspond to simulations involving an even number of imprecise flips (θ + 360°). (e)-(f) Experimental CODEX curves of the non-protonated ^{13}C (e) and protonated ^{13}C (f) and fits (solid lines) that include contributions from both small angle oscillations (dotted lines) and ring flips (dashed line). Adapted with permission from Ref [52]. Copyright 2003 American Institute of Physics.

In 2005, Bloise and co-authors utilized ^{13}C CODEX and DIPSHIFT NMR to measure the main chain and side chain motions, respectively, in poly[2-methoxy,5-(2'-ethylhexyloxy)-p-phenylenevinylene] (MEH-PPV). [53] The order parameter, *S*, taken as the intensity of a DIPSHIFT curve at half the rotor period ($t_r/2$) ranges from 0 to 1 for isotropic motion and no motion, respectively, in the 10^{-3} s to 10^{-6} s time range. As shown in Figure 15.4a,b the aromatic ring (C2 and C5), vinyl bond (C7 and C9), and side chain methylene adjacent to the backbone (C10) exhibit order parameters approximately equal to one from 215 to 320 K, indicating no appreciable main chain motion in the 10^{-3} s to 10^{-7} s time scale. As given in Figure 15.4b, the side chain carbons C12-C16 exhibit S values less than one that decrease with increasing temperature. The methyl and methoxy carbons (C9, C15, C17, see Figure 15.4a) exhibited extremely fast motions ($0.15 < S < 0.35$). Assuming the motion of the C-H bond at the branch point methane carbon (C11) was diffusion on a cone, the cone amplitude increased from 14° to 42° upon increasing temperature from 243 K to 323 K.

As shown in Figure 15.4c, CODEX showed that the average correlation times of the main chain carbons (triangles; C1, C3, C4, C6) were identical (90 ms) with a broad distribution of correlation times, $\beta = 0.4$, corresponding to three decades in time, indicating that the main chain motion was heterogeneous. When performed as a function of dephasing time (Figure 15.4d), it was found that the tilt angle of reorientation of the main chain carbons is 25°. Since this motion is much slower (90 ms) than the electron transfer processes that give rise to electroluminescence (10^{-12} s to 10^{-9} s), this molecular tilt angle distribution was taken to be static. Blue shifts in the photoluminescence spectra between 220 K to 320 K have been associated with increases in chain disorder, which agrees overall with the CODEX measurements. Heating over 220 K causes β-relaxations, which were correlated with large amplitude motions of the side chains that cause dissociation of intrachain excitons.

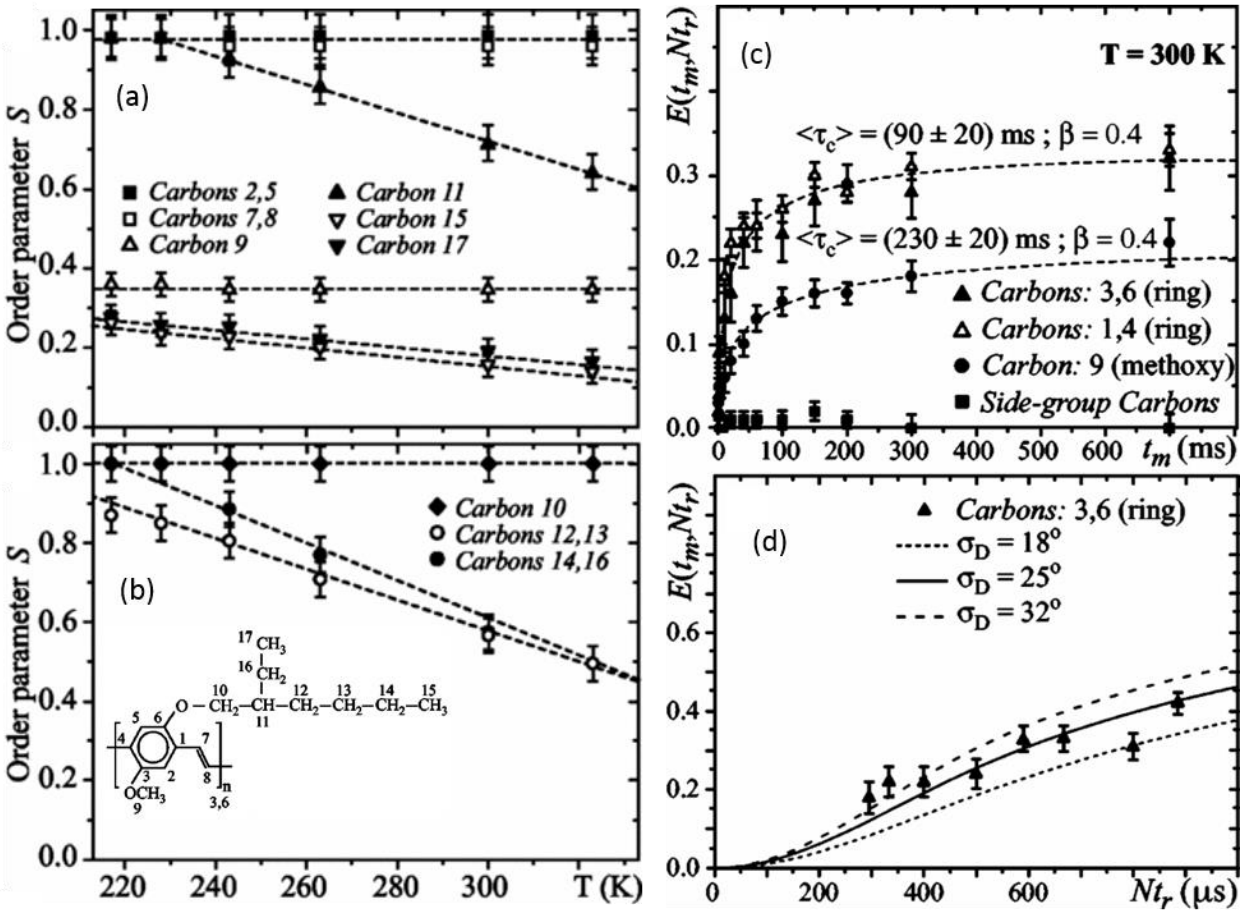

Figure 15.4: (a)-(b): DIPSHIFT order parameters as a function of temperature for the protonated ^{13}C of PPV. (c) CODEX curves as a function of mixing time (t_m) for the phenylene ring carbons (triangles), methoxy (circles) and side chain (squares) carbons. (d) CODEX exchange intensity as a function of the dephasing time (Nt_r) for the ring carbons (C3, C6) and CODEX simulations for different oscillation angles. Reprinted Figure 2 and Figure 4 with permission from Ref. [53]. Copyright 2005 by the American Physical Society.

Polyalkythiophenes (PATs) are polymers that have potential uses as transistors and as p-type semiconductors in OPVs. Studies on PATs have shown a significant dependence of carrier mobility on main chain order and paracrystallinity [54], so establishing precise metrics of polymer structure and dynamics is important for understanding the physics behind charge transport. Furthermore, since PATs

are semi-crystalline understanding crystallization behaviors at the molecular scale is critical for optimizing film deposition protocols and ultimately predicting morphologies. In 2006, Yazawa and coworkers published differential scanning calorimetry (DSC) and ^{13}C NMR results taken on powders of poly(3-butylthiophene) (P3BT) (Figure 15.5) and Fourier transform infrared (FTIR) of films of P3BT. [55] The DSC (Figure 15.5a) showed endothermic peaks at 340 K and 550 K; the former disappeared upon annealing at 423 K for 3 minutes but reappeared and increased in intensity after storing at 298 K with increasing storage time. P3BT was assigned as a plastic crystal and the low temperature transition was ascribed to a “twist glass” transition, but alternatively has been assigned as a “normal” crystal in the mesophase classification scheme by Wunderlich. [12,56,57] Little appreciable change was observed in the ^{13}C NMR spectra upon heating 298 K to 373 K in the aromatic region (Figure 15.5c), but a notable change was observed for the methyl C4’ peak at 15 ppm (Figure 15.5d). The FTIR of the C4 thiophene out-of-plane stretching region, which is sensitive to backbone motions, changed significantly upon heating from 300 K to 400 K (Figure 15.5b).

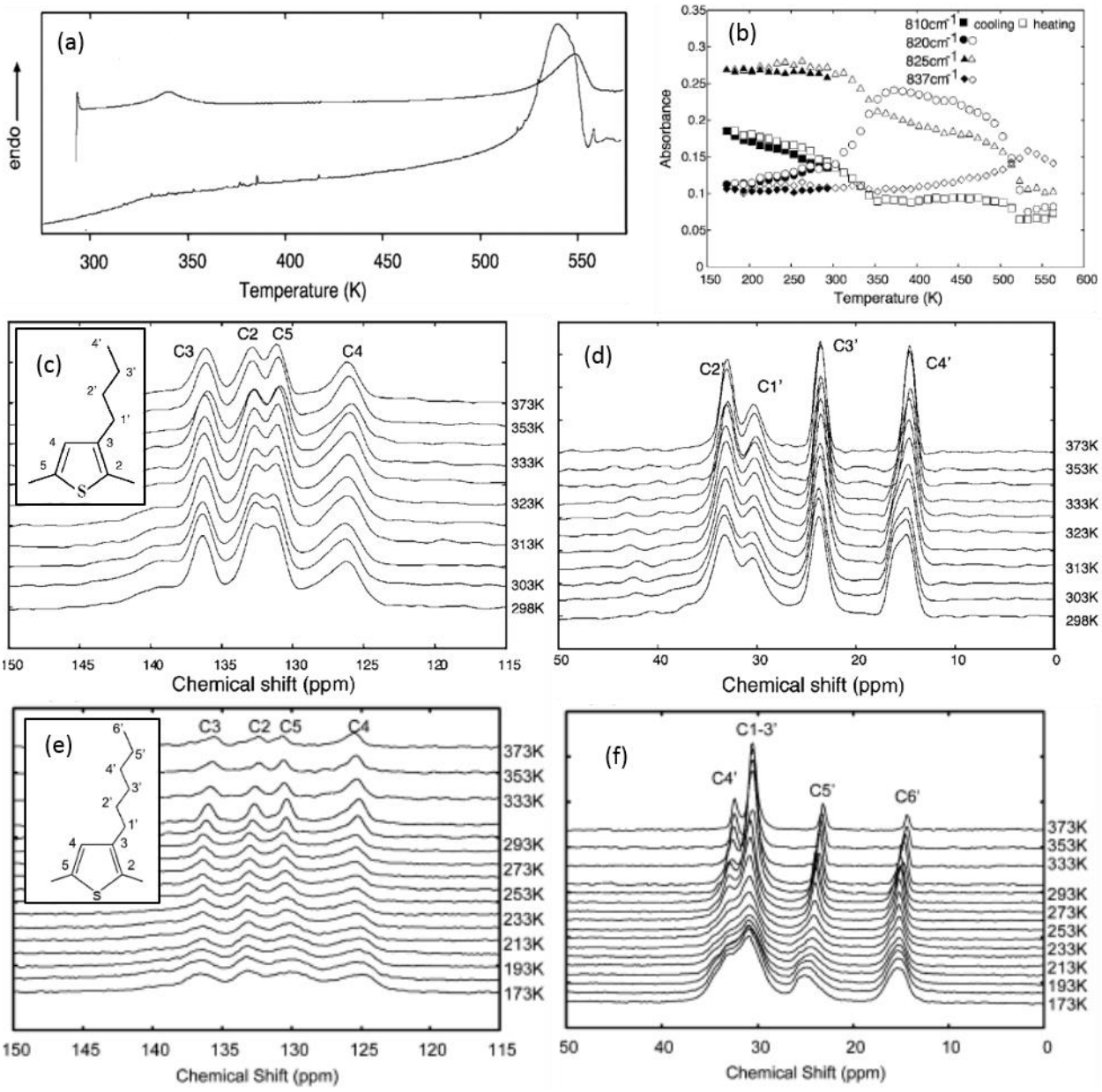

Figure 15.5: (a) DSC traces for P3BT including the first scan (top) and second scan (bottom). (b) FTIR absorbance intensity of P3BT as a function of temperature. (c)-(d) ^{13}C CPMAS spectra of P3BT for various temperatures. (e)-(f) ^{13}C CPMAS spectra of P3HT for various temperatures. Reprinted figure with permission from Ref. [55]. Copyright 2006 by the American Physical Society.

In a follow up study in 2010, Yazawa et al. reported UV-Vis optical absorption, FTIR, and ^{13}C CPMAS-based T_{1C} relaxation experiments on poly(3-hexyl thiophene) (P3HT) as a function of temperature. [58] The FTIR and UV-Vis experiments were performed on drop-cast films from chloroform and the NMR experiments on as-received powders. Three peaks were observed in the optical absorption spectra (515, 560, and 615 nm) that red shifted with increasing temperatures, indicating increasing dynamic disorder. There were no appreciable changes observed in the FTIR spectra of the C-H alkyl stretching band in this temperature range, which, based on the peak position, indicated gauche conformations of the side chains. In the ^{13}C CPMAS spectra of the as-received powders, broad resonances were observed at cold temperatures for all ten carbons (side chain and main chain carbons), which narrowed upon heating (Figure 15.5e,f). Upfield shifts were observed for the hexyl carbons upon heating, most notably the methyl and ε-methylene carbons, which were ascribed to the γ-gauche effect of increasing gauche populations of methylene chain conformers upon heating. Variable temperature (173 K to 373 K) ^{13}C T_1 experiments showed that the relaxation of the side chain methyl carbons were in the fast fluctuation limit (τ_c < 2 ns = 1/500 MHz) and the main chain carbons in the slow fluctuation limit (τ_c > 2 ns = 1/500 MHz). The side chain methylene carbons show T_1 relaxation maxima (where τ_c = 2 ns) at 253 K, 273 K, and 293 K for the methylene units that are five, four, and one-to-three bonds away from the main chain, respectively.

Pascui and coworkers examined a pair of low molecular weight P3HT powders (M_n = 3 kDa and 6 kDa) with ^{13}C magic angle spinning (MAS) and ^{13}C-^{1}H DIPSHIFT experiments for various temperatures. [59] As observed by Yazawa et al. [58], upon increasing temperature upfield shifts were observed for the methyl and methylene peaks (Figure 15.6a). There were two methyl peaks observed at 15 and 14 ppm that were assigned to chains in the crystal and non-crystal phases, respectively, and the observed upfield shifts demonstrated that (time averaged) trans-rich to gauche-rich conformational changes occur

upon heating. The NMR-determined crystallinity was calculated based on structures that have P3HT units with well-ordered side-chain arrangements.

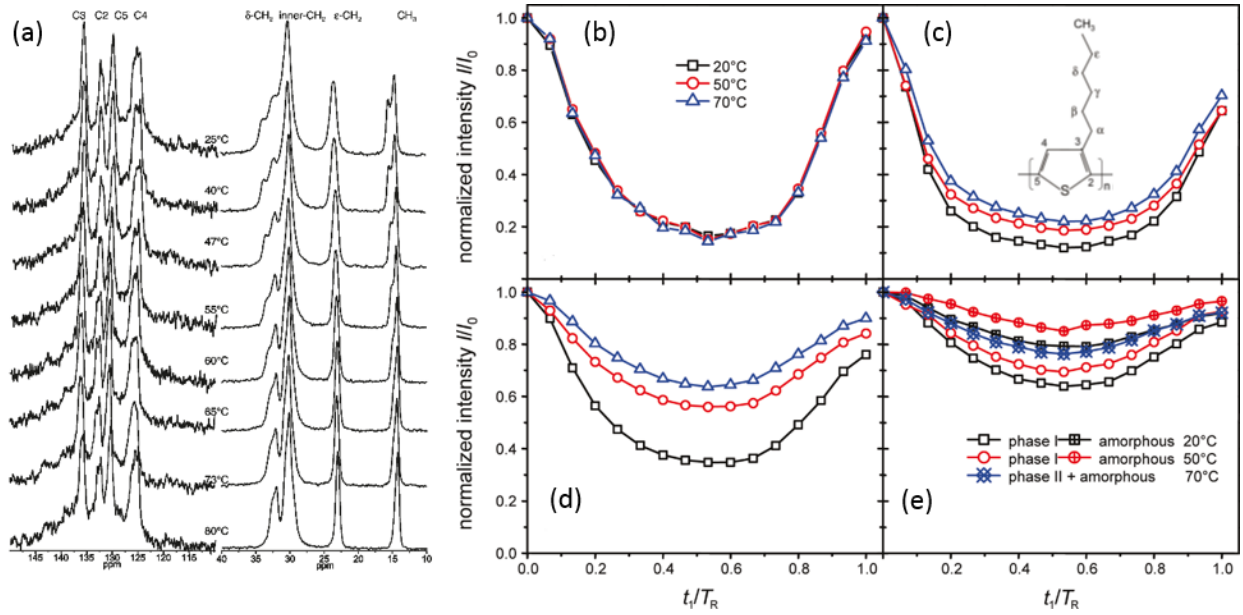

Figure 15.6: (a) ^{13}C MAS NMR spectra of 3 kDa P3HT for various temperatures. (b)-(d) ^{13}C-^{1}H DIPSHIFT curves for 3 kDa P3HT for the thiophene C4 carbon (b), β-, γ-, and δ-CH_2 (c), ε-CH_2 (d), and methyl carbons for various temperatures. Adapted with permission from Ref [59]. Copyright 2010 American Chemical Society.

Dynamics in the mid-kHz frequency scale were investigated with DIPSHIFT experiments. The high scaling factor (0.79) of the main chain carbon (C4) suggested no appreciable main chain reorientations (Figure 15.6b) even at temperatures T_g + 20°C, T_g + 50°C, and T_g + 70°C (e.g., T_g = 0°C). The dynamics of the side chain interior methylene (Figure 15.6c) and ε-methylene (Figure 15.6d) C-H bonds showed clear temperature dependences with the more rigid interior methylenes exhibited dynamic scaling factors ranging from 0.65 to 0.85 and the ε-methylene bonds ranging from 0.35 to 0.65. The methyl carbons,

which exhibited different peaks corresponding to crystal and non-crystal phases, were the most mobile ($0.1 < S < 0.3$) and exhibited scaling factors depending on phase and temperature, demonstrating that the amplitudes of the side chain motions were smaller in the crystal than in the amorphous phase.

In 2012, Dudenko and coworkers reported on results of ^{1}H double quantum – single quantum (DQ-SQ) MAS and ^{13}C-^{1}H heteronuclear correlation (HETCOR) experiments of P3HT. [60] DQ-SQ NMR probes the proximity of two proton spins; the proximity depends on the recoupling time. In the ^{1}H DQ-SQ reported by Dudenko et al, a short recoupling time was used to measure only the strong couplings at short ranges (< 4.0 Å). As shown in Figure 16.4a, an autocorrelation peak was observed for the crystalline thiophene resonance at 6.0 ppm. Since the closest distance between protons on the same chain is > 4.0 Å, the correlation was due to intermolecular contacts. Nuclear independent chemical shift (NICS) calculations on $(3HT)_6$ tetramers predicted 1.0 to 1.6 ppm upfield shifts depending on packing structure, which agreed well with the shift observed in experiment for the crystalline resonance (6.0 ppm) relative to the non-crystal resonance (6.9 ppm). Furthermore, the upfield ^{1}H shift of the crystalline thiophene resonance in the ^{1}H spectrum was correlated with upfield shifts of the ^{13}C thiophene resonances (Figure 16.4b).

In 2017, Bohle et al. proposed that 2D ^{1}H-^{1}H DQ-SQ correlation spectroscopy and nuclear independent chemical shift (NICS) simulations could be used to constrain packing motifs in poly(3-alkyl thiophenes) (P3ATs). [61] As shown earlier by Dudenko et al. [60], since correlations arise for strong two-spin dipolar couplings only (spins within 4 Å), and since intramolecular main chain proton-to-proton distances are > 4 Å, autocorrelation peaks must be intermolecular (Figure 16.4a). As a result, specific packing motifs were proposed in which (1) the thiophene protons are to within 4.0 Å of one another, and (2) the thiophene protons exhibit a ≈1 ppm upfield shift via NICS simulation (Figure 16.4e). Using

these constraints, the authors proposed packing motifs in which adjacent intermolecular thiophene units are staggered and the chains are tilted by 20˚ in the crystal phase.

In 2014, Nieuwendaal and coworkers showed variable temperature ^{13}C CPMAS of high molar mass P3HT that exhibited broad ^{13}C resonances at low temperatures that narrow upon heating to temperatures > 0°C (Figure 15.7c) [62] as observed previously by Yazawa et al. [58] The broadening observed at low temperatures was ascribed to disorder (conformational inhomogeneity) in both the side chain and main chain moieties, and the narrowing upon heating > 0°C was ascribed to fast fluctuations that serve to average these conformational inhomogeneities on < 3 ms time scales. Recall from DIPSHIFT measurements from Pascui et al. [59] that S = 0.79 for 3 kDa P3HT. In order to recitify the two studies, the > 0°C fluctuations must (1) only involve main chain reorientations that would only slightly dynamically average the C4-H dipolar coupling (S = 0.79), or (2) be dependent on molar mass. The Nieuwendaal et al study also showed that $T_{1\rho}^{H}$-based spectral editing could be utilized to quantitatively separate ordered and disordered fractions observed from ^{13}C CPMAS spectra (Figure 15.7a,b) of high molar mass P3HT. Due to disagreement between the crystallinity estimates based on raw melt enthalpy values from DSC (8.9 and 21 J/g) and from NMR (0.47 and 0.55), it was surmised that ordered chains may exist in the non-crystalline phase. [62] However, in a 2014 follow-up study using P3HT of various molecular weights, the same research group reported that the ^{13}C NMR-based ordered fractions matched DSC-determined crystal fractions when accounting for surface enthalpic effects by using the Gibbs-Thomson equation and enthalpy and melt temperature values estimated in the infinite chain limit. These results showed that ^{13}C CPMAS NMR could be used for quantitatively measuring P3HT crystallinity and that the raw melt enthalpy value should not be used for calculating crystallinity. [63] Experimental details of the NMR measurement were described later by Nieuwendaal et al. [64] A paper by Xhen et al. showed that $T_{1\rho}^{H}$-based spectral edited ^{13}C CPMAS could reliably be utilized for crystallinity quantitation even with significant spinning sideband intensity. [65]

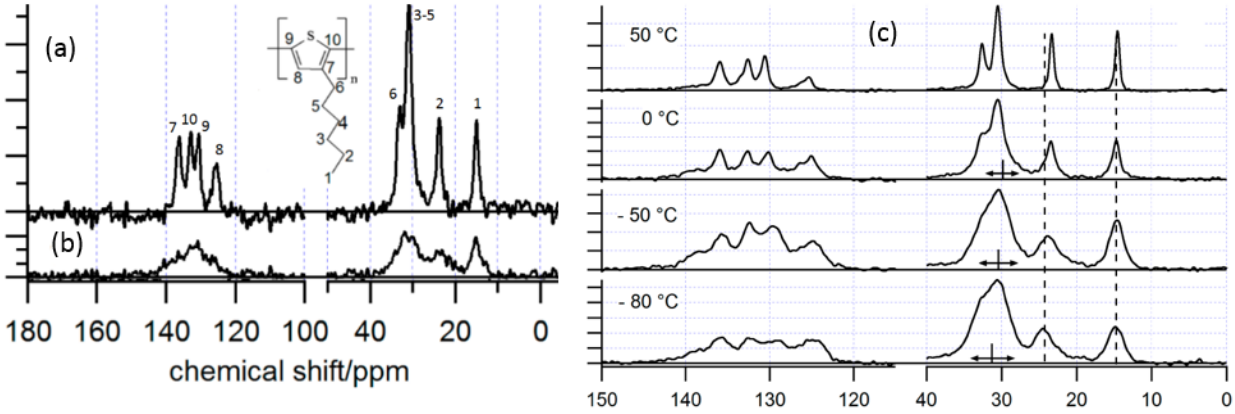

Figure 15.7: ^{13}C CPMAS NMR of P3HT: (a) ordered P3HT, (b) disordered P3HT, and (c) for various temperatures. A chemical structure of P3HT is given, along with the resonance assignments. Adapted with permission from Ref [62]. Copyright 2014 American Chemical Society.

In 2016, Yuan and coworkers showed ^{13}C CPMAS spectra of P3BT films drop-cast from chloroform and CS_2 and showed two forms (Figure 15.8a). [66] Upon annealing the chloroform-deposited film, the ^{13}C resonance at 126 ppm split into two resonances. FTIR spectra were taken of the films that exhibited distinguished features: the chloroform-cast films exhibited bands at 811, 819, 825, and 832 cm^{-1}, whereas the CS_2-cast film exhibited bands at 825, 832, and 845 cm^{-1} (Figure 15.8b).

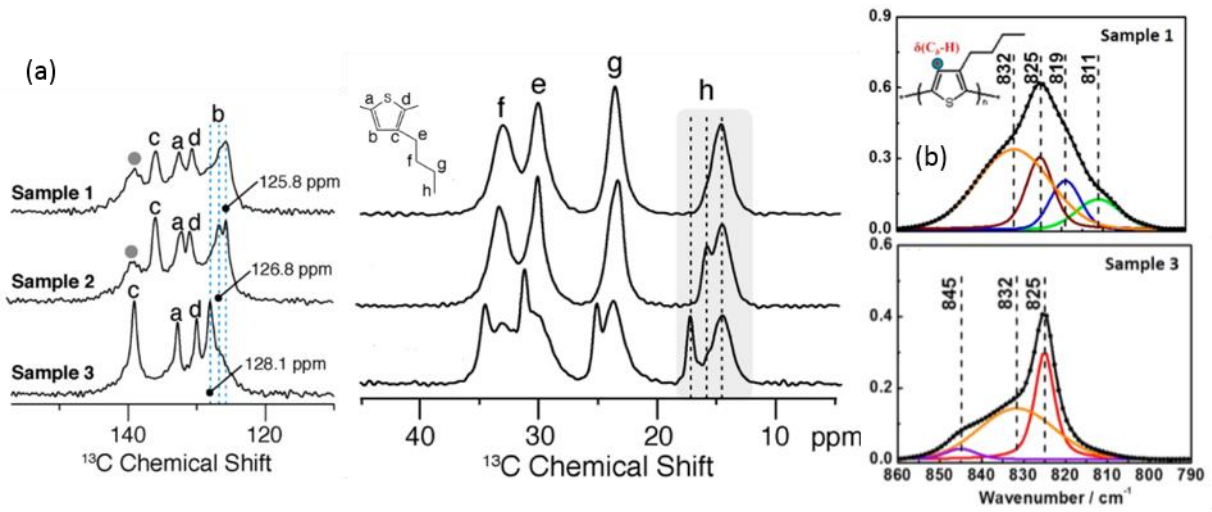

Figure 15.8: (a) ^{13}C CPMAS spectra of P3BT cast from chloroform (top), cast from chloroform and annealed (middle), and cast from CS_2 (bottom). (b) FTIR spectra of P3BT cast from chloroform (top) and CS_2 (bottom). Adapted with permission from Ref [66]. Copyright 2016 American Chemical Society.

In 2018, Zhang et al. examined the effects of side chain length on main chain packing in P3BT with ^{13}C NMR and FTIR. [67] P3ATs of four different side chain lengths (n = 3, 5, 7, 11, Figure 15.9a) were studied. As reported originally by Dudenko and coworkers [60], ^{13}C {^{1}H} HETCOR showed correlations between the amorphous phase ^{13}C and ^{1}H resonances (138 ppm, 6.8 ppm) and between the crystalline phase resonances (136 ppm, 6.0 ppm). The P3BT C2 carbon exhibited two peaks at ≈125 ppm whereas the other three P3ATs exhibit a single C2 peak (Figure 15.9b). There were no other appreciable changes on the thiophene carbon lineshapes and positions. As given in Figure 15.9c, P3BT exhibited four peaks in the FTIR out-of-plane thiophene C-H vibration region (800 cm^{-1} to 860 cm^{-1}) whereas the other three P3ATs exhibited two or three peaks. The FTIR bands between 806 and 825 cm^{-1} were assigned to different conformations in the crystalline phase with varying degrees of side chain order, the FTIR band at 830 cm^{-1} to 833 cm^{-1} was assigned to disordered P3HT, and the 825 cm^{-1} band was assigned to a

mesophase as in the previous study [66], but no additional phases were observed in the ^{13}C CPMAS NMR and no DSC data was given to support the claim.

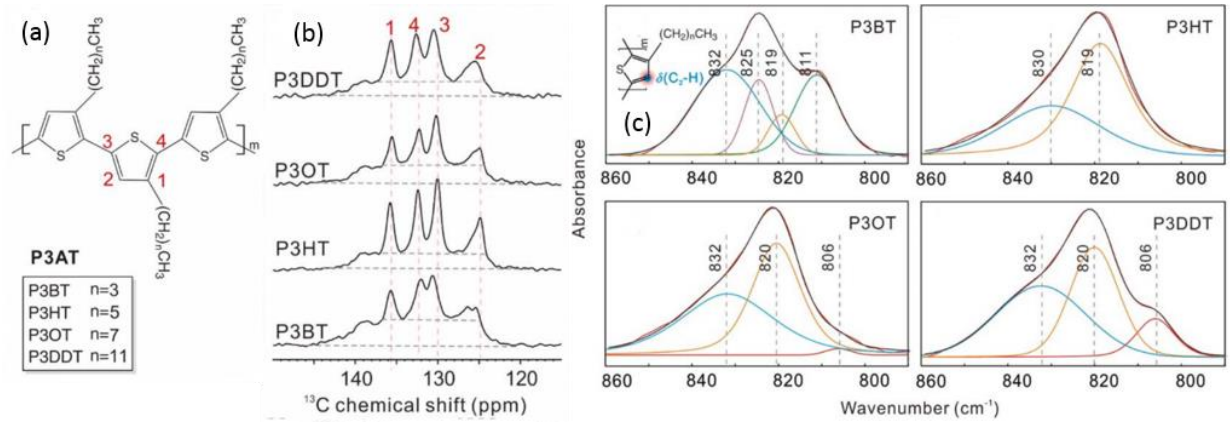

Figure 15.9: (a) Schematic of P3AT. (b) ^{13}C CPMAS spectra of P3ATs of various side chain lengths. (c) FTIR spectra of various P3ATs. The peak at 138 ppm is likely due to non-crystalline chains as reported in Ref. [63]. Adapted with permission from Ref. [67]. Copyright 2016 John Wiley and Sons.

In 2017, Melnyk and coworkers utilized ^{1}H and ^{13}C NMR to study poly(2,5-bis(3-tetradecyl-thiophen-2-yl)thieno[3,2-b]thiophene) (PBTTT), including rotor encoded rotational echo double resonance (REREDOR) NMR to study side chain dynamics. [68] PBTTT has been reported as a highly crystalline (> 80 %) semicrystalline polymer [69] with (1) interdigitated crystalline side chains that that melt in the temperature range 50 – 150°C and (2) a crystal-to-liquid crystal transition in the temperature range 220 – 280°C. [12] The chemical structure of PBTTT is given in Figure 15.10a, including a schematic of the 16 methylene unit side chain. Linefitting of the thiophene resonances in the ^{1}H spectra was used for estimating main chain order (Figure 15.10b), and linefitting the aliphatic carbons in the ^{13}C MAS spectra was used for determining trans/gauche conformer populations of the side chain carbons (Figure 15.10c). Three populations were assumed, a crystalline phase, in which the main chain and side chains were

ordered; a mesophase, in which the main chain was ordered, but side chain was disordered; and an amorphous phase, in which both the main chain and side chains were disordered. The dynamic order parameters of the dipolar couplings were measured via REREDOR for the side chain methylene C-H bonds (Figure 15.10d,f), and via REPT-HDOR for the main chain protons (Figure 15.10g,h). The dynamic order parameters of the backbone thiophene and thienothiophene were high, 0.93 and 0.89, respectively, indicating a rigid backbone; recall the order parameter measured for P3HT by Pascui et al. [59] using DIPSHIFT was 0.79 showing greater main chain mobility likely as a result from dynamic coupling to the more highly mobile hexyl side chains of P3HT as compared to PBTTT. Side chain interior methylenes in the trans-trans conformation were relatively rigid (0.71), whereas methylenes further from the backbone were more dynamic (0.65, 0.49). The terminal methyl was the most dynamic (0.39). Amorphous side chain methylenes exhibited lower order parameters, by approximately a factor of 2.

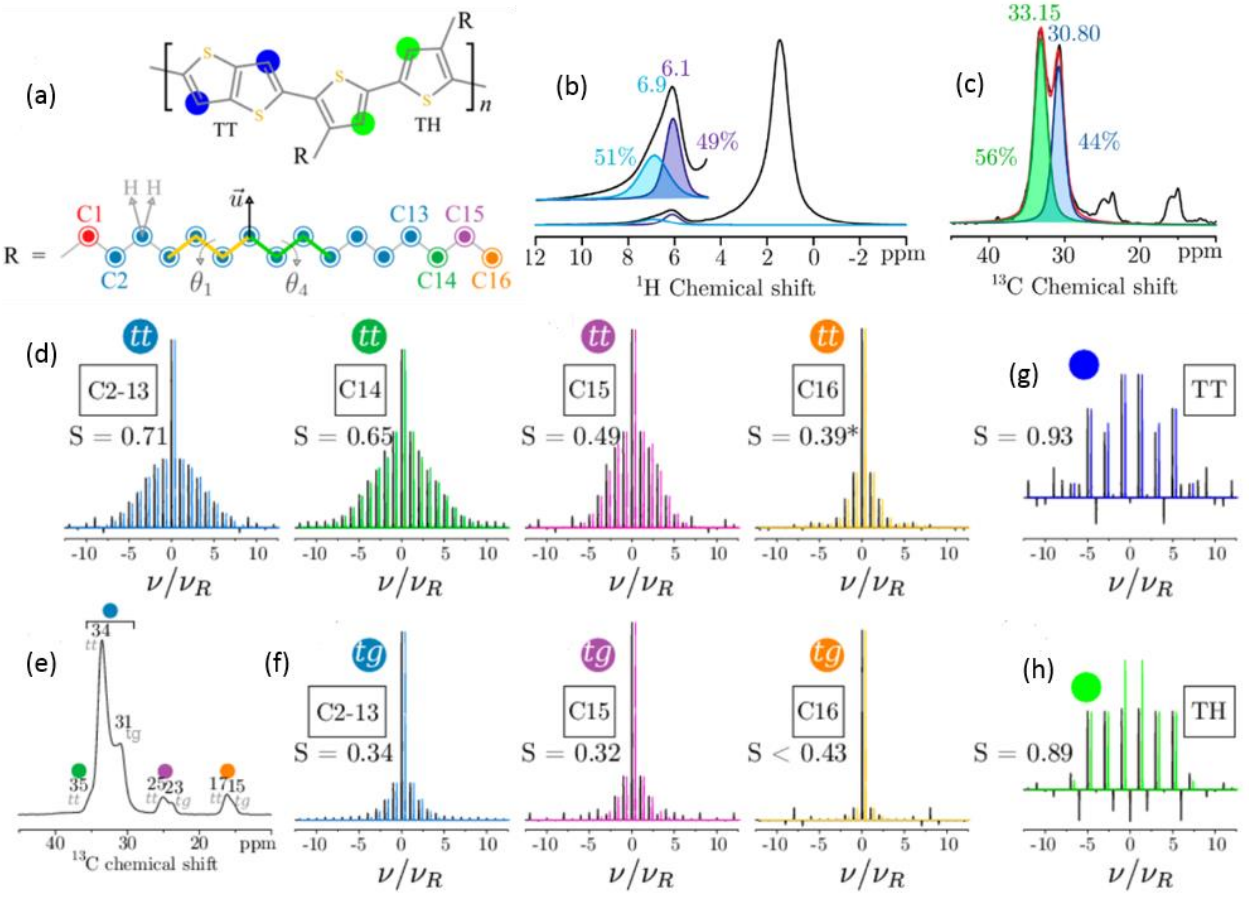

Figure 15.10: (a) Chemical structure of PBTTT. (b) ^{1}H NMR spectrum of PBTTT. (c) ^{13}C NMR spectrum of PBTTT. (d),(f) Experimental REREDOR patterns of the various side chain carbons corresponding to a trans-trans "tt" conformation (d) and trans-gauche "tg" conformation (f), and ^{13}C NMR spectrum showing the assignments (e). REPT-HDOR patterns of protonated ^{13}C corresponding to PBTTT monomers with trans-trans (g) and trans-gauche (h) side chain conformers. Adapted with permission from Ref [68]. Copyright 2017 American Chemical Society.

15.2.3 Donor-acceptor polymers

An emerging class of polymers has been developed that rely on alternating units of conjugated monomers in order to tailor the absorption wavelength, π orbital overlap, and charge transport for optimal device function. [70,71] These copolymers, so-called "donor-acceptor" polymers, have resulted

in tremendous strides for a number of OE metrics, including carrier mobilities and OPV power conversion efficiencies. [72] Donor-acceptor polymers offer a new route for synthetically tailoring the organic layer to fit the device function. However, due to the increased monomer sizes, establishing structure-property-processing relationships can be more challenging: the increased atom number per monomer increases the number of local packing configurations. Furthermore, the conjugation length, which is dictated by chain rigidity and local packing and dynamics, is an important parameter in determining the optical absorption as well as the carrier mobility. Hence, it is important to establish metrics that can address these various details regarding structure and dynamics. In 2013, Faria and coworkers reported on X-ray diffraction (XRD), DSC, dynamic mechanical thermal analysis (DMTA), dielectric spectroscopy, and ^{13}C DIPSHIFT results of poly(9,9-di-n-octyl-fluorene-alt-benzothiadiazole), or F8BT, a copolymer that has applications in transistors and n-type semiconductors for OPVs due to its potentially high carrier mobilities. [73] A chemical structure of F8BT is given in Figure 15.11a. DMTA showed a β-transition at 193 K and a T_g at 385 K, the latter of which was also observed via DSC. Current-voltage (I-V) measurements were performed over this temperature range to investigate the charge transport in F8BT, in particular the presence of "traps," which are mid-level energy states that restrict charge motion. The I-V mesaurements showed that the trap density distribution narrows and the overall trap density increases close to the glass transition, which was ascribed to increasing polymer backbone torsion. ^{13}C-^{1}H DIPSHIFT experiments performed for various temperatures (Figure 15.11b) revealed that the side chain methylene C-H bonds undergo motions with an activation barrier of 0.3 eV to 0.23 eV (Figure 15.11c) for the interior and end-adjacent methylene bonds, respectively, which agreed well with the value from frequency-dependent DMTA (0.27 eV).

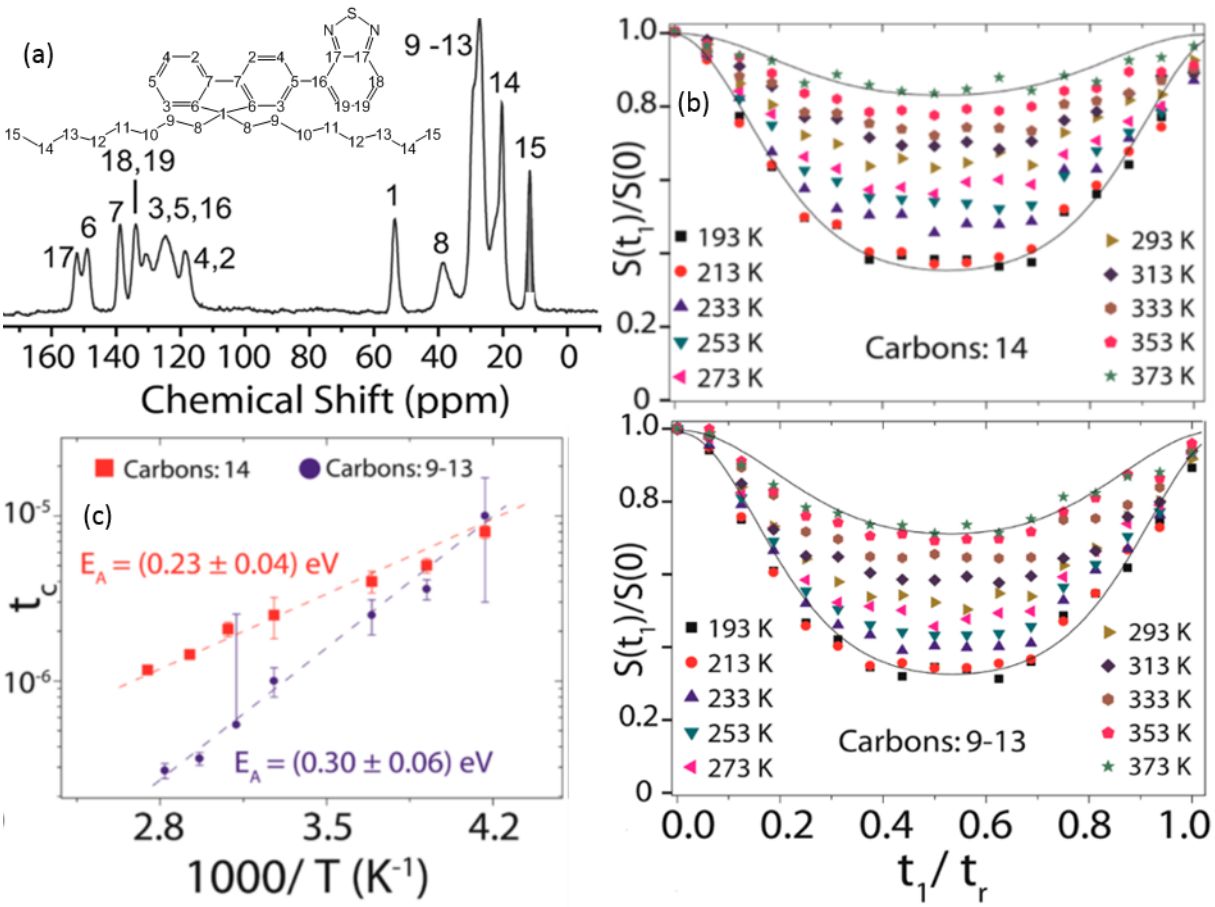

Figure 15.11: (a) ^{13}C CPMAS spectra of F8BT. (b) ^{13}C-^{1}H DIPSHIFT curves of the (b) interior methylene carbons and (d) the ε-methylene carbons. (d) Arrhenius plots of the correlation times for the side chain carbons. Adapted with permission from Ref [73]. Copyright 2013 American Chemical Society.

Establishing methods that can measure chain packing arrangements in donor-acceptor polymers are important for quantifying the impacts of chain rigidity and orbital overlap on carrier mobilities. There have been multiple reports of using multidimensional NMR for probing atom connectivities in donor-acceptor polymers. In principle, ^{13}C NMR-based methods, such as 2D ^{13}C CODEX [30] or ^{13}C-detect REDOR [74], exhibit the cleanest spectral separation between resonances, but require relatively large amounts of sample (>100s mg), isotopic labeling, and/or unreasonable signal averaging times.

Alternatively, ^{1}H-^{1}H correlation experiments can be used to probe proximities with no isotope labeling, but the primary disadvantage is that resolution (≈1 ppm) is rarely sufficient to cleanly separate individual peaks of similar moieties (i.e. thiophene vs. aromatic protons). Spectral resolution can be much improved in ^{13}C-^{1}H HETCOR [75,76], but the dual requirements of efficient ^{1}H-to-^{13}C polarization transfer and sufficient ^{1}H resolution can make the experiment a challenge. Absolute ^{13}C intensity can be complicated by the dependence of the ^{1}H-to-^{13}C cross-polarization kinetics on the Hartmann-Hahn match conditions, MAS rate, and B_1 inhomogeneity. For HETCOR using Hartmann-Hahn pulses for polarization transfer and fast MAS to improve ^{1}H resolution, polarization transfer is typically slow/non-quantitative at fast MAS; further, ^{1}H-^{1}H mixing during the ^{1}H-to-^{13}C polarization transfer can result in uncertainty in ^{1}H-^{13}C correlation assignments since they can be either direct (^{1}H-^{13}C) or indirect (i.e., ^{1}H-to-^{1}H-to-^{13}C) couplings. ^{1}H combined rotation and multiple pulse (CRAMPS) decoupling [77] methods such as Lee Goldburg-based decoupling [78] can be used during polarization transfer as well as during the ^{1}H evolution to reduce the number of indirect correlations as well as improve ^{1}H resolution, respectively. However, one ambiguity arises in that the CRAMPS scaling factor can effect the ^{1}H chemical shift scale which can (1) result in uncertainty in the absolute ^{1}H peak position and (2) shift NMR intensity to unrealistic regions of the ^{1}H spectrum (< 0 ppm). [79] In these cases, it is paramount to quantify the effects of pulse amplitude drift and probe tuning on phase transients, which thereby effect the scaling factor.

Tsao and coworkers utilized ^{1}H-^{1}H DQ-SQ NMR on a cyclodithiophene (CDT)-benzothiadiazol (BTZ)-based donor-acceptor polymer, which showed clear correlations between main chain protons (8 and 6 ppm) and adjacent side chain methylene protons (Figure 15.12a). [80] DQ-based NMR experiments probe the proximities of two proton spins. The 8 ppm resonance exhibited no appreciable autocorrelation peak intensity, but the 6 ppm resonance did, albeit slightly shifted downfield to 6.5

ppm, indicating that the downfield shoulder of the two benzothiadiazole protons are due to more strongly dipolar coupled protons than those correlated to the peak in the ^{1}H spectrum at 6.0 ppm.

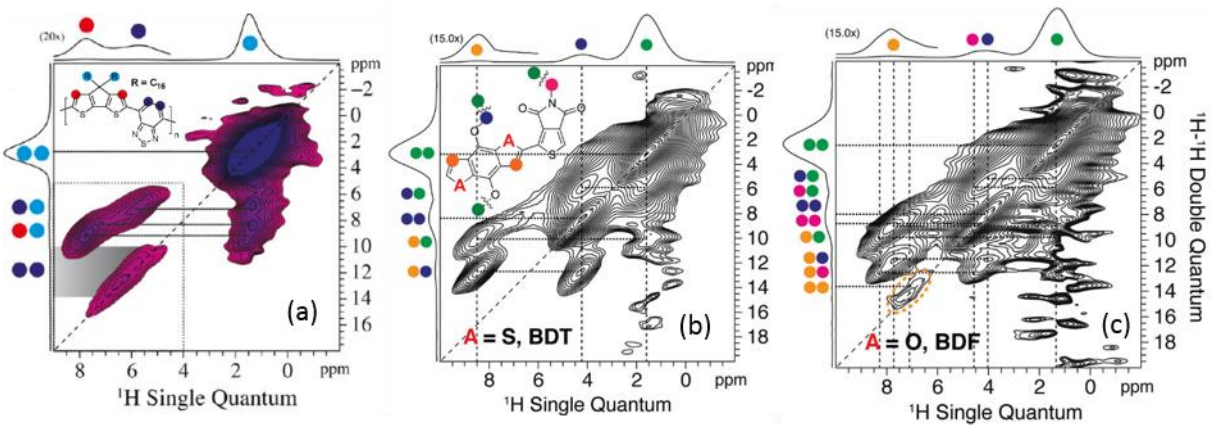

Figure 15.12: ^{1}H DQ-SQ MAS NMR contour plots of CDT-BZT (a), PBDTTPD (b), and PDFTPD (c). Reprinted with permission from Ref [80]. Copyright 2011 American Chemical Society.

In 2016, Do et al. utilized ^{1}H-^{1}H DQ-SQ and TQ-SQ correlation experiments to probe proton proximities and backbone tacticities for a pair of benzodithiophene-thiophene copolymers both with and without fluorination in poly(4,8-bis((2-ethylhexyl)-oxy) benzo[1,2-b:4,5-b']dithiophene-thiophene (PBDT[2H]T), and the 3,4-difluoro-thiophene analog (PBDT[2F]T), respectively. [81] DQ-SQ correlation experiments revealed no appreciable difference between the two polymers (Figure 15.13a,b). Recall that DQ-SQ NMR measurements probe proximities of proton spin pairs. The TQ-SQ experiment, which probes the proximities of *three* proton spins within a 4 Å radius, showed correlations for the thiophene backbone protons for the protonated form (Figure 15.13c), but not the fluorinated form (dotted circle, Figure 15.13d), showing differences in molecular packing between the two copolymers.

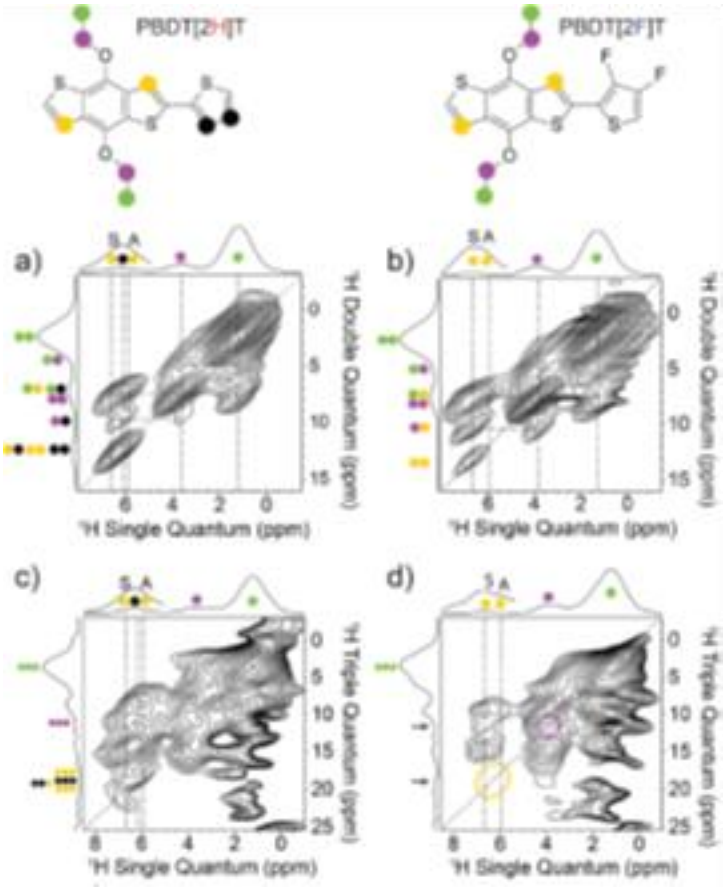

Figure 15.13: (a)-(b) ^{1}H DQ-SQ correlation contour plots of PBDT[2H]T (a), and PBDT[2F]T (b). (c)-(d) ^{1}H TQ-SQ contour plots of PBDT[2H]T (c) and PBDT[2F]T (d). Adapted with permission from Ref. [81]. Copyright 2016 John Wiley and Sons.

In 2016, Wang et al. utilized ^{1}H DQ-SQ correlation experiments on two benzo [1,2-b:4,5-b'] dithiophene–6,7-difluoroquinoxaline polymers with two different donor/acceptor arrangements. [82] As shown in Figure 15.14a, the SM3 copolymer exhibits a clear autocorrelation peak for the pair of thiophene protons (Figure 15.14a, two red dots at 5.7 ppm) as well as correlation peaks between the thiophene proton resonances at 7.7 and 6.8 ppm (Figure 15.14a, red and orange dots). Signal intensity on the diagonal at 7.6 ppm was ascribed to autocorrelations of the 7.6 ppm peak (Figure 15.14a, green

dots) and intermolecular proton-proton dipolar couplings, although there was significant spectral overlap with the off-diagonal peak at 7.7 ppm (FWHM > 1.0 ppm).

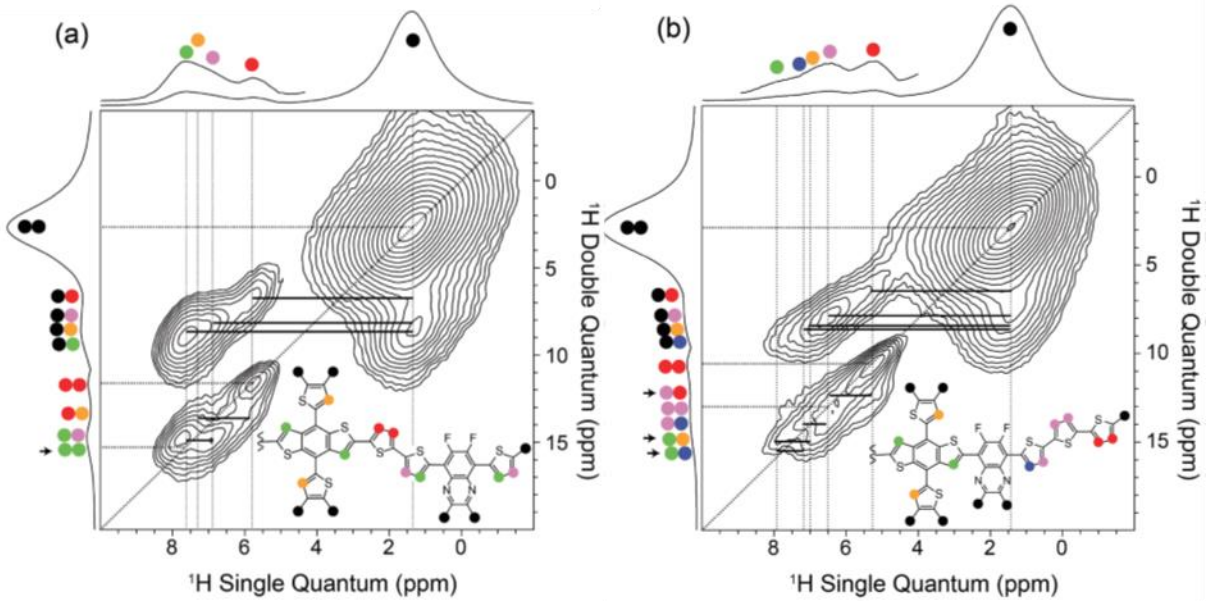

Figure 15.14: ^{1}H DQ-SQ contour plots of polymers SM3 (a) and SM1 (b). The chemical structures with assignments are included as insets. Adapted with permission from Ref. [82]. Copyright 2016 John Wiley and Sons.

Like SM3, the SM1 polymer exhibited a peak maximum along the diagonal at SQ = 5.2 ppm (Figure 15.14b, two red dots) that corresponds to the two protons an isolated thiophene (Figure 15.14b, red dots on chemical structure) and a shoulder at 6.5 ppm that was also due to two protons on an isolated thiophene (Figure 15.14b, purple dots on chemical structure). There was significant spectral overlap at SQ > 6 ppm (4 resonances within 2 ppm), but the authors noted that the off-diagonal intensity at both SQ = 8 ppm and 7 ppm on the shoulder of the peak at SQ $\approx$ 6.5 ppm could be ascribed to intermolecular proton-proton dipolar couplings, which is suggestive of different packing motif from that of the SM3 copolymer.

In 2017, Chaudhari et al. utilized ^{1}H DQ-SQ correlation NMR (Figure 16.6a) and molecular simulations to constrain polymer chain conformations and stacking arrangements in films of the donor-acceptor polymer poly(diketopyrrolo-pyrrole-dithienylthienothiophene) (DPP-DTT) (Figure 16.6b). [83] DFT calculations were performed on monomer segments (Figure 16.6c) and the NMR chemical shifts were calculated from the geometry optimized structures in a periodic structure using CASTEP methods including NICS effects. Two structures were proposed (types I and II) and the simulated resonances of type II matched experiment closer than did type I in both the ^{1}H and ^{13}C MAS spectra (Figure 16.6d).

In 2017, Lo et al. utilized ^{1}H DQ-SQ NMR to probe proton connectivities in a set of fused dithiophene-co-thienopyrrolodione polymers that included carbon, silicon, or germanium as the thiophene-fused atom (Figure 15.15a). [84] Of the three polymers studied, only the polymer with carbon bridging thiophene units showed no autocorrelation peak observed for one rotor period (Figure 15.15b) or four rotor periods (Figure 15.15c) of DQ recoupling, which is due to a lack of proximity of intermolecular thiophene units. The other two polymers clearly exhibited the autocorrelation peaks (dotted circles, Figure 15.15d-g). Interestingly, the DSC of the as-synthesized powders revealed that only the carbon-bridging polymer exhibited no crystal melting endotherm, whereas the other two polymers did.

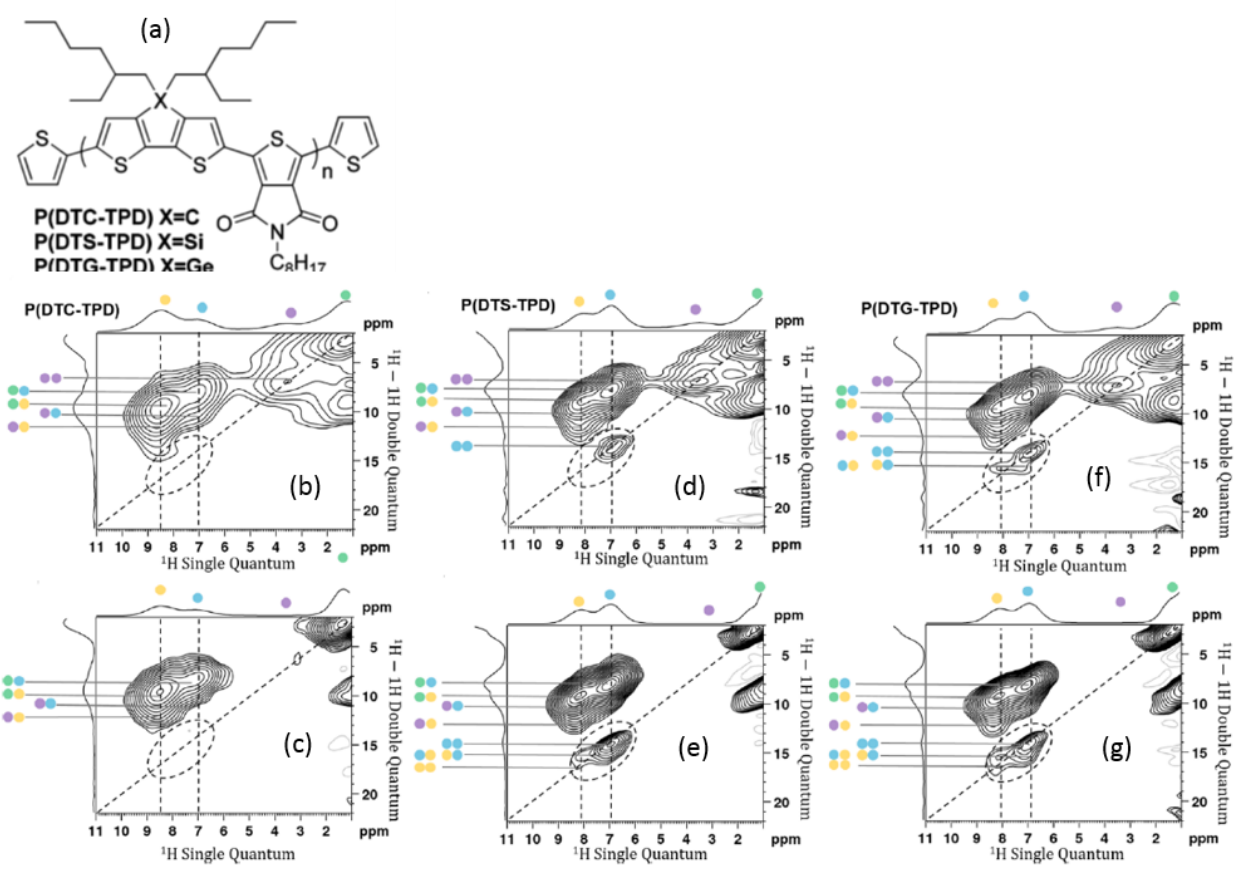

Figure 15.15: (a) Chemical structure of P(DTX-TPD). (b)-(g) ^{1}H DQ-SQ NMR contour plots for P(DTC-TPD) (b,c), P(DTS-TPD) (d,e), and P(DTG-TPD) (f,g). Spectra (b), (d), (f) were recorded using one rotor period of DQ recoupling, and (c), (e), (g) were recorded using four. Adapted with permission from Ref [84]. Copyright 2018 American Chemical Society.

15.2.4 Polymer blends for organic photovoltaics

The active layer in an OPV device, better known as the bulkheterojunction (BHJ) layer, is a thin film blend of p-type and n-type semiconducting organic molecules. [85,86] BHJs must be thin (< 1 μm) due to their high optical aborption and highly mixed due to the short exciton radius (< 10 nm). BHJ layers are typically fabricated via casting from a single solution, so donor/acceptor miscibility and cosolubility with a common solvent are critical parameters for optimizing the morphology. Flory-Huggins parameters for

donor and acceptor molecules have been reported. [87,88] Optimized BHJs should be mixed on < 10 nm length scales so as to achieve high interfacial surface area for maximum charge extraction. Hence, it is critical to quantitatively measure the domain sizes in the BHJ; one powerful method for measuring domain sizes in polymer blends is ^{1}H spin diffusion NMR. In 2010, Nieuwendaal et al. utilized ^{1}H spin diffusion NMR to measure the coarsening of drop-cast blends of P3HT/PCBM after thermal annealing. [89] The ^{1}H CRAMPS spectra of P3HT, PCBM, and the P3HT/PCBM blend are given in Figure 15.16(a)-(d). In the ^{1}H spin diffusion experiment the pulse sequence establishes spectra that are multipled by a sine wave (Figure 15.16d) yielding positive and negative polarizations (i.e. a gradient) that dissipate due to spin diffusion and reduce in intensity (Figure 15.16(e)-(h)). In the limit of Fickian spin exchange dynamics, the slope of this decay rate can be related to a domain size: rapid spin polarization exchange between the two components in the blend is indicative of fine mixing (high interfacial area) and slow spin exchange is indicative of larger domains (lower interfacial area). The ^{1}H spin diffusion NMR plots of the drop-cast P3HT/PCBM films exhibited a range of slopes depending on thermal annealing demonstrating that domains existed over a large range of size scales (1 nm to > 100 nm). The as-cast film (solid squares, Figure 15.16i) exhibited a steep initial slope to $\Delta M = 0.4$, indicating that 60% of the film ((1 – 0.4) x 100%) was mixed at < 5 nm size scales. Furthermore, domains grew when annealed at 150° and 180°C (triangles and open circles, Figure 15.16i, respectively), but not at 100°C (open squares, Figure 15.16i), due to PCBM crystallization. Extensive annealing at 180°C resulted in incomplete phase separation, suggesting that the coarsened PCBM crystals did not completely sequester the PCBM from the P3HT-PCBM mixed phase. PCBM is known to quench P3HT fluorescence upon fine mixing, and the quantitative changes in blend coarsening from the NMR correlated well with photoluminescence quenching experiments.

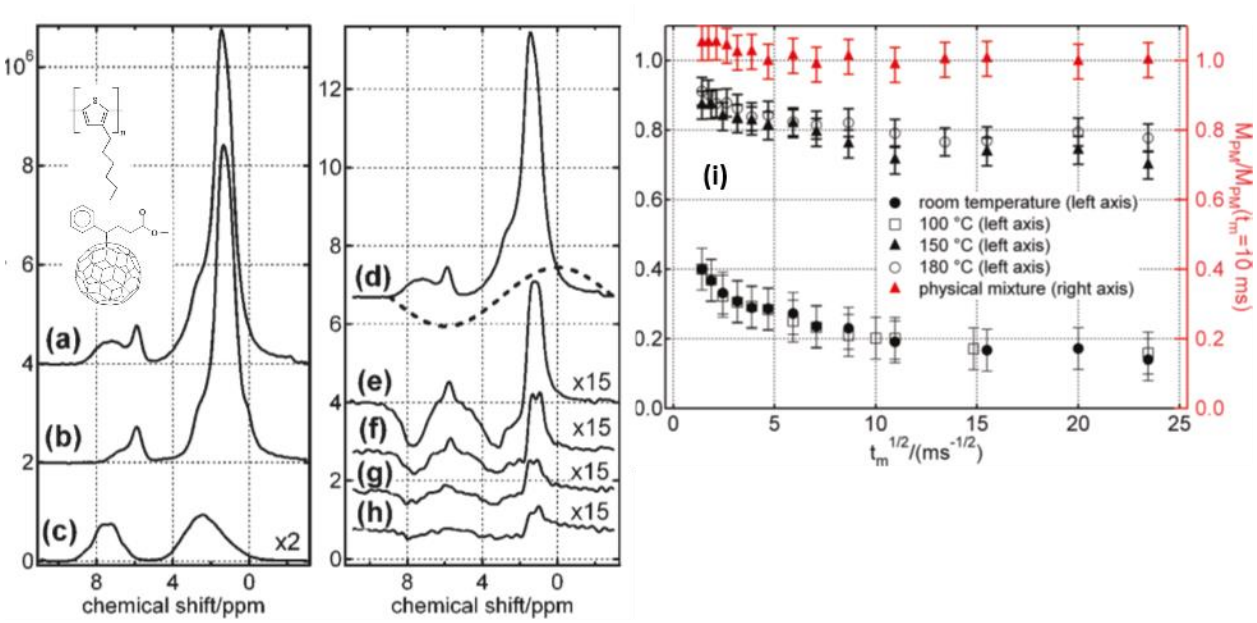

Figure 15.16: (a)-(d) ^{1}H CRAMPS spectra of (a) P3HT-PCBM, (b) P3HT, (c) PCBM. (d) is a repeat of (a) showing the spectrum is multipled by a sine wave as guide for the eye. (e)-(h) ^{1}H spin diffusion spectra of P3HT/PCBM for mixing times of 2 ms (e), 60 ms (f), 180 ms (g), and 550 ms (h). (i) ^{1}H spin diffusion plots of various samples of P3HT-PCBM. Adapted with permission from Ref [89]. Copyright 2010 American Chemical Society.

In a 2012 follow-up study, Nieuwendaal and coworkers reported ^{1}H NMR results of ≈80 nm films of P3HT-PCBM spun-cast from o-dichlorobenzene for OPV devices fabricated using various processing conditions. [90] Again, ^{1}H CRAMPS-based spin diffusion was used to measure the domain size distributions in films cast for different drying rates both with and without thermal annealing (Figure 15.17a-i). As depicted in the ^{1}H spin diffusion plots (Figure 15.17j), fast initial slopes were observed for all four films indicative of small (< 5 nm) domains in the mixed phase and the more gradual slopes observed at longer times, which were ascribed to long-scale composition heterogeneity that resulted from variations in the casting process.

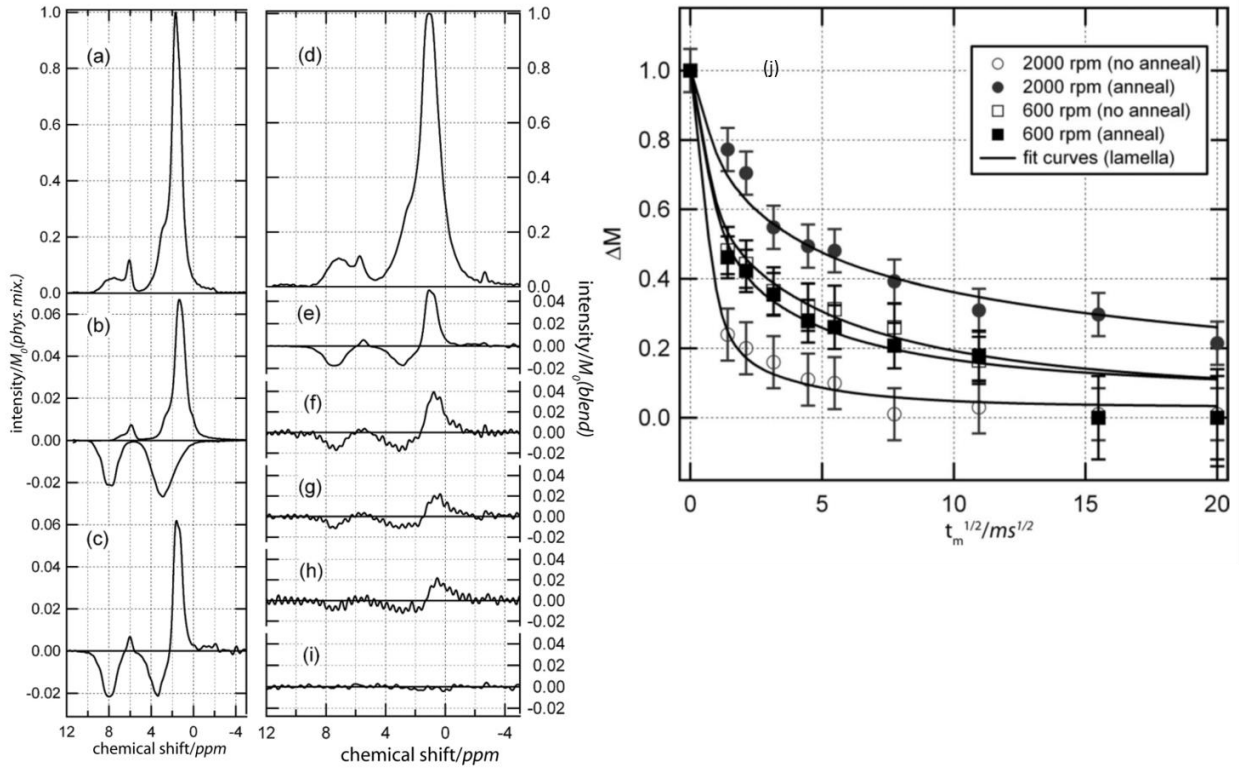

Figure 15.17: (a), (b), (d): ^{1}H CRAMPS NMR spectra of a 50:50 physical mixture of P3HT:PCBM (a), a thin film 50:50 blend of P3HT:PCBM (d), and neat P3HT and PCBM with positive and negative polarizations (b). (c), (e)-(i): ^{1}H CRAMPS spin diffusion NMR spectra of a physical mixture ((c) and (e)), and a thin film for mixing times of 2 ms (f), 30 ms (g), 60 ms (h), and 240 ms (i). (j) A spin diffusion plot of four thin films of P3HT:PCBM for various processing conditions. Adapted with permission from Ref. [90]. Copyright 2012 John Wiley and Sons.

In 2011, Mens et al. examined blends of poly(2-methoxy-5-(30,70-dimethyl octyl oxy)-1,4-phenylene-vinylene) (MDMO-PPV) and phenyl-C61butyric acid methyl ester (PCBM) with ^{13}C, ^{1}H $T_{1\rho}^{H}$ and T_1^{H} relaxometry with ^{13}C NMR detection. [91] ^{13}C spin lattice relaxation time (T_{1C}) measurements of the C_{60} resonance (starred peak, Figure 15.18b,c) revealed both a fast and a slow component; the former due to PCBM in highly-dynamic proton-rich regions, the latter to PCBM in more rigid, proton-dilute

regions. For the blends, the slow component was assigned to weakly organized PCBM nanoclusters, and the fast component was assigned to PCBM in the mixed phase. However, a fast T_1^C relaxation was observed in the absence of the polymer (Table 1, 0/100 ratio), clouding the mixed phase assignment. If correct, then the mixed phase fraction could be quantitatively calculated (Molar ratio in the mixed phase, Table 1). These assignments were utilized in a follow-up study on P3HT/PCBM doctor bladed films to show that the mol% of PCBM in "nanocrystals" was 35% when cast from chlorobenzene and 51% when cast from toluene. [92]

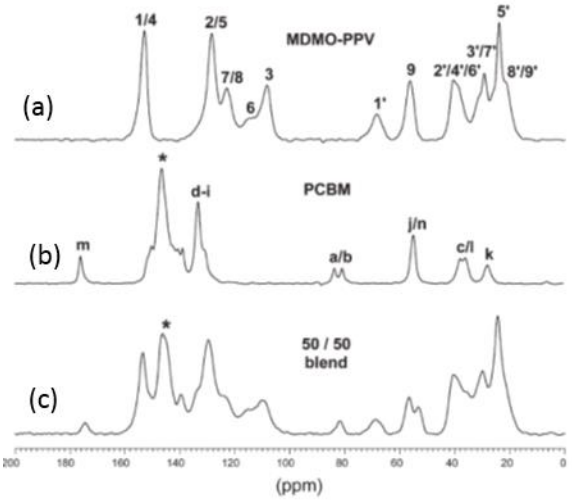

Figure 15.18: (a) ^{13}C CPMAS spectra of MDMO-PPV (a), PCBM (b), and their 50/50 blend (b). Adapted from Ref. [91].

Weight ratio (wt %) PCBM	80/20	50/50	20/80	15/85	0/100
Molar ratio	93/7	76/24	44/56	36/64	0/100
T_{1C} (s)	16.3	11.6 (73 %)	11.5 (50 %)	10.0 (36 %)	11.2 (26 %)
		40.2 (27 %)[a]	41.3 (50 %)[a]	42.0 (64 %)[a]	42.7 (74 %)[a]
Molar ratio in the mixed phase[b]	-	100/23	100/64	100/64	-

Table 1: T_{1C} relaxation decay times observed for 150 nm thick doctor bladed films of PCBM and MDMO-PPV/PCBM cast from chlorobenzene for various compositions. The T_{1C} was measured from the C60

resonance (146 ppm). The mol % of nanoclustered PCBM and the molar ratio of MDMO-PPV/PCBM in the mixed phase are listed. (a) mol % of PCBM in nanoclusters. (b) Molecules of PCBM expressed over 100 repetition units of MDMO-PPV.

In 2015, Etzold et al. examined both poly[2,6-(4,4-bis-(2-ethylhexyl)-4H-cyclopenta[2,1-b;3,4-b']-dithiophene)-alt-4,7-(2,1,3-benzothiadiazole)] (PCPDTBT) and its Si analog (PSPDTBT) blended with PCBM by using 2D ^{13}C {^{1}H} HETCOR NMR to determine relative proximities of the donor and acceptor molecules. [93] Correlation peaks were observed between the aliphatic side chain carbons and aromatic protons for the PCPDTBT:PCBM blend with no additive (Figure 15.19b), but not for the PCPDTBT:PCBM blend with octadecanethiol additive (Figure 15.19c) or the PSPDTBT:PCBM blend with no ODT additive (Figure 15.19d). No such correlation was observed for the neat PCPDTBT polymer. These correlations, which are due to ^{13}C-^{1}H dipolar couplings, were ascribed to PCPDTBT aliphatic ^{13}C proximal to PCBM aromatic protons and could result from higher polymer/PCBM interfacial area of that specific blend, differences in molecular packing at the interface, or differences in polymer side chain dynamics between the blends.

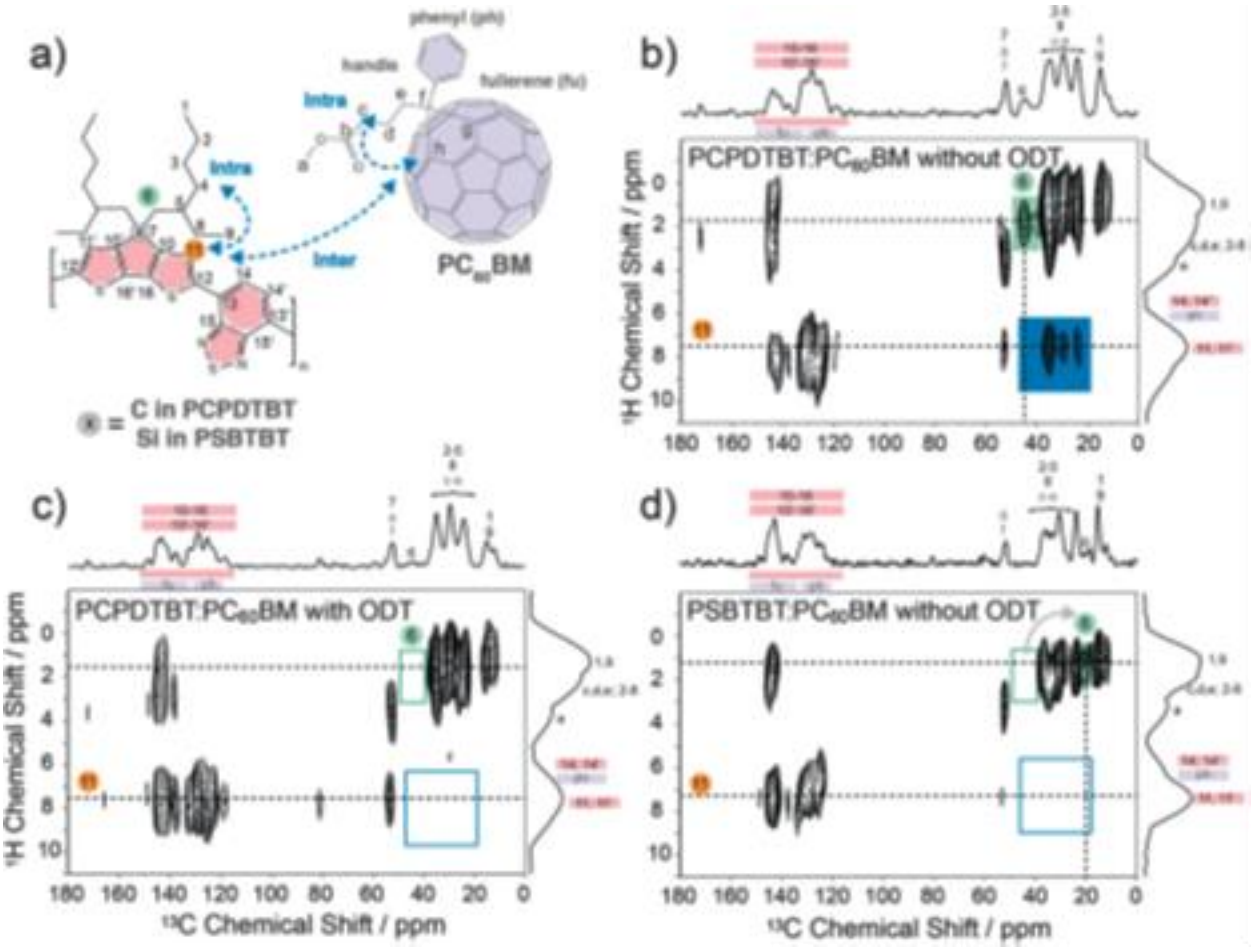

Figure 15.19: (a) The chemical structures of PCPDTBT and PCBM with the colors corresponding to assignments in the HETCOR plots. (b)-(d) ^{13}C-^{1}H HETCOR spectra of PCPDTBT:PCBM without ODT (b), PCPDTBT:PCBM cast with ODT (c), and PSPDTBT:PCBM without ODT (d). Adapted from Ref. [93].

In 2018, Nieuwendaal et al. utilized ^{13}C {^{2}H} rotational echo double resonance (REDOR) NMR to quantitatively measure ^{13}C-^{2}H dipolar couplings at the P3HT/PCBM interface in an ≈80 nm thin film bulk heterojunction blend of ^{13}C-enriched-fullerene PCBM and ^{2}H-enriched-thiophene P3HT that was doctor bladed from chlorobenzene. [94] ^{1}H spin diffusion NMR of the film showed ≈80 % of the film was composed of a mixed phase with domain sizes < 6 nm, similar to the unannealed spun-cast films from their earlier study (open circles, Figure 15.17j). [90] Unfortunately, similar to that initial study

intramolecular spin equilibration and uncertainty in the topology/dimensionality of the components in the mixed phase precluded more precise estimates of domains in the mixed phase from ^{1}H spin diffusion alone. As given in Figure 15.20a, the C60 resonance is the most intense peak in the ^{13}C CPMAS spectrum ("S_0") of the thin film blend and is attenuated upon application of ^{2}H dephasing pulses due to ^{13}C-^{2}H dipolar dephasing ("S"). When plotting the intensity as a function of number of dephasing pulses (or dephasing time), the rate of dephasing can be used to calculate the dipolar coupling, and ultimately the internuclear distance on < 1 nm length scales. Alternatively, if there are multiple dipolar couplings, then the dephasing rate can be used to probe different spin configurations. In this study, the distances and the numbers of ^{2}H nuclei surrounding the fullerene ^{13}C were evaluated by placing PCBM in a simple cuboid model as depicted in Figure 15.20b. REDOR curves were calculated using this model for (1) three different cuboid lengths (1.6, 1.66, and 1.72 nm), (2) thiophenes in either the edge-on or face-on orientation with respect to the fullerene, and (3) numbers of thiophenes on the faces of the cube (one to six, see Figure 15.20b legend). The experimental curve had a slower slope than would be expected from the calculated curve based on the mixed phase composition, which proved neat ≈2 nm PCBM clusters existed in the mixed phase. Furthermore, when using a bimodal fit of of neat PCBM cuboids ($\Delta S = 0$) and mixed component cuboids ($\Delta S > 0$), it was shown that the absolute amount of interfacial surface area to volume (0.10 ± 0.02 $Å^{-1}$) and the fraction of donor/acceptor contacts (0.3) are relatively insensitive to the cuboid dimensions and molecular orientations used in the model, whereas the fraction of >2 nm-sized PCBM clusters in the mixed phase is known less precisely. The spatial correlation function was calculated from the best fit model of the REDOR data, which correlated well with small angle neutron scattering (SANS) experiments.

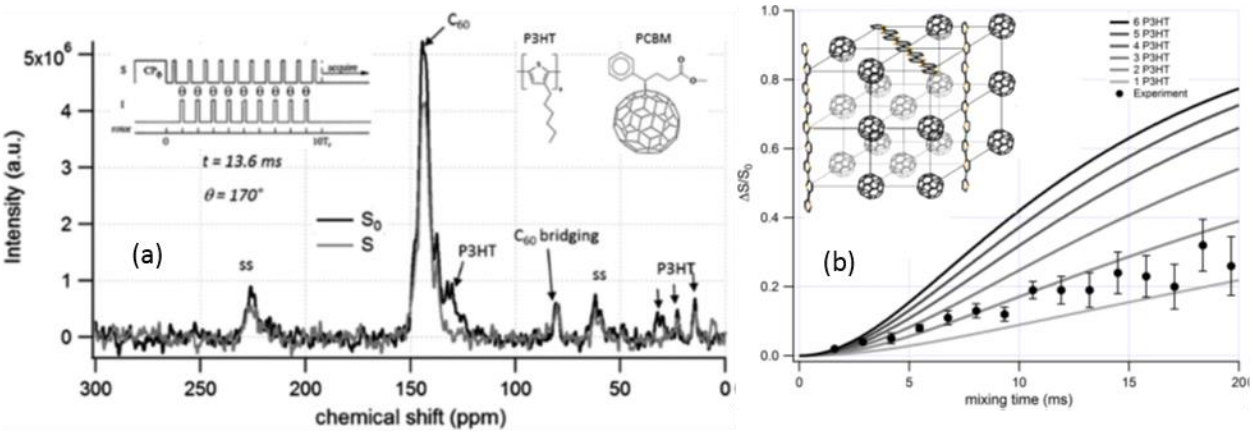

Figure 15.20: (a) ^{13}C {^{2}H} REDOR NMR spectra both with (S) and without (S_0) ^{2}H dephasing pulses. (b) Experimental ^{13}C {^{2}H} REDOR dephasing curve of a P3HT:PCBM BHJ thin film (circles) and REDOR simulations using a simple cuboid model with a central fullerene surrounded by P3HT. The simulations shown are for varying numbers of P3HT on the cube faces (one through six). Reprinted figure with permission from Ref [94]. Copyright 2018 by the American Physical Society.

15.3 Summary

Solid-state NMR is a powerful method for probing local structure and dynamics in heterogeneous films used for OE applications. There are libraries of experiments to select from depending on the application and the question to be answered. The molecular dynamics, which can have important implications with charge transport physics, can be measured with high chemical specificity and over a wide range of time scales (10^{-6} to 10^{0} s) when using ^{13}C-^{1}H DIPSHIFT and ^{13}C CODEX experiments. The molecular orientation distribution can be measured using the CSA pattern in oriented films, and crystallinity can be measured using ^{13}C MAS NMR. Differences in molecular packing in donor-acceptor polymers or polymer blends can be observed by ^{1}H-^{1}H or ^{1}H-^{13}C correlation experiments. The size scales of mixing and mixed phase fraction in a polymer blend can be measured via ^{1}H spin diffusion methods and via ^{1}H and ^{13}C relaxation experiments. The amount of donor-acceptor interfacial area and number of

donor/acceptor contacts in a BHJ, which is important for modeling efficiency, can be quantitatively measured via REDOR.

15.4 References

1 H. Shirakawa, *Synth. Met.*, 1995, 6.
2 J. D. Yuen and F. Wudl, *Energy Environ. Sci.*, 2013, **6**, 392.
3 A. F. Paterson, S. Singh, K. J. Fallon, T. Hodsden, Y. Han, B. C. Schroeder, H. Bronstein, M. Heeney, I. McCulloch and T. D. Anthopoulos, *Adv. Mater.*, 2018, **30**, 1801079.
4 Y. Yamashita, F. Hinkel, T. Marszalek, W. Zajaczkowski, W. Pisula, M. Baumgarten, H. Matsui, K. Müllen and J. Takeya, *Chem. Mater.*, 2016, **28**, 420–424.
5 R. A. Street, *Phys. Rev. B*, 1983, **27**, 4924–4932.
6 S. S. Li and W. R. Thurber, *Solid-State Electron.*, 1977, **20**, 609-616.
7 N. D. Arora, J. R. Hauser and D. J. Roulston, *IEEE Trans. Electron Devices*, 1982, **29**, 292–295.
8 L. Meng, Y. Zhang, X. Wan, C. Li, X. Zhang, Y. Wang, X. Ke, Z. Xiao, L. Ding, R. Xia, H.-L. Yip, Y. Cao and Y. Chen, *Science*, 2018, **361**, 1094–1098.
9 K. Yoshikawa, H. Kawasaki, W. Yoshida, T. Irie, K. Konishi, K. Nakano, T. Uto, D. Adachi, M. Kanematsu, H. Uzu and K. Yamamoto, *Nat. Energy*, 2017, **2**, 17032.
10 R. J. Kline, M. D. McGehee, E. N. Kadnikova, J. Liu, J. M. J. Fréchet and M. F. Toney, *Macromolecules*, 2005, **38**, 3312–3319.
11 F. C. Spano, *J. Chem. Phys.*, 2005, **122**.
12 C. R. Snyder, R. J. Kline, D. M. DeLongchamp, R. C. Nieuwendaal, L. J. Richter, M. Heeney and I. McCulloch, *J. Polym. Sci. Part B Polym. Phys.*, 2015, **53**, 1641–1653.
13 K. Gu, C. R. Snyder, J. Onorato, C. K. Luscombe, A. W. Bosse and Y.-L. Loo, *ACS Macro Lett.*, 2018, **7**, 1333–1338.
14 B. T. O'Connor, O. G. Reid, X. Zhang, R. J. Kline, L. J. Richter, D. J. Gundlach, D. M. DeLongchamp, M. F. Toney, N. Kopidakis and G. Rumbles, *Adv. Funct. Mater.*, 2014, **24**, 3422–3431.
15 D. Gargi, R. J. Kline, D. M. DeLongchamp, D. A. Fischer, M. F. Toney and B. T. O'Connor, *J. Phys. Chem. C*, 2013, **117**, 17421–17428.
16 X. Zhang, H. Bronstein, A. J. Kronemeijer, J. Smith, Y. Kim, R. J. Kline, L. J. Richter, T. D. Anthopoulos, H. Sirringhaus, K. Song, M. Heeney, W. Zhang, I. McCulloch and D. M. DeLongchamp, *Nat. Commun.*, , DOI:10.1038/ncomms3238.
17 D. . VanderHart and F. Khoury, *Polymer*, 1984, **25**, 1589–1599.
18 W.-G. Hu, C. Boeffel and K. Schmidt-Rohr, *Macromolecules*, 1999, **32**, 1611–1619.
19 D. Hentschel, H. Sillescu and H. W. Spiess, *Polymer*, 1984, **25**, 1078–1086.
20 E. Pérez and D. L. Vanderhart, *J. Polym. Sci. Part B Polym. Phys.*, 1987, **25**, 1637–1653.
21 W. L. Earl and D. L. VanderHart, *J. Am. Chem. Soc.*, 1980, **102**, 3251–3252.
22 G. E. Maciel, W. L. Kolodziejski, M. S. Bertran and B. E. Dale, *Macromolecules*, 1982, **15**, 686–687.
23 R. H. Atalla and D. L. Vanderhart, *Science*, 1984, **223**, 283–285.
24 H. Miura, J. Hirschinger and A. D. English, *Macromolecules*, 1990, **23**, 2169–2182.

25 D. L. VanderHart, A. Asano and J. W. Gilman, *Macromolecules*, 2001, **34**, 3819–3822.
26 M. Bertmer, M. Wang, M. Krüger, B. Blümich, V. M. Litvinov and M. van Es, *Chem. Mater.*, 2007, **19**, 1089–1097.
27 K. Schmidt-Rohr, *Science*, 1998, **280**, 714–717.
28 J. Schaefer, E. O. Stejskal, R. A. McKay and W. T. Dixon, *Macromolecules*, 1984, **17**, 1479–1489.
29 P. L. Lee and J. Schaefer, *Macromolecules*, 1995, **28**, 1921–1924.
30 M. Singh and J. Schaefer, *J. Am. Chem. Soc.*, 2011, **133**, 2626–2631.
31 M. Mehring and J. Spengler, *Phys. Rev. Lett.*, 1984, **53**, 2441–2444.
32 R. A. Wind, H. Lock and M. Mehring, *Chem. Phys. Lett.*, 1987, **141**, 283–288.
33 F. Hentsch, M. Helmle, D. Köngeter and M. Mehring, *Phys. Rev. B*, 1988, **37**, 7205–7208.
34 F. Rachdi, T. Nunes, M. Ribet, P. Bernier, M. Helmle, M. Mehring and M. Almeida, *Phys. Rev. B*, 1992, **45**, 8134–8137.
35 G. Zimmer, A. C. Kolbert, M. Mehring, F. Rachdi, P. Bernier and M. Almeida, *Phys. Rev. B*, 1993, **47**, 763–768.
36 J. Shinagawa, Y. Kurosaki, F. Zhang, C. Parker, S. E. Brown, D. Jérome, J. B. Christensen and K. Bechgaard, *Phys. Rev. Lett.*, 2007, **98**, 147002.
37 K. Kanoda, *Hyperfine Interact.*, 1997, **104**, 235–249.
38 L. Mandelkern, *Crystallization of Polymers*, Cambridge University Press, 2nd edn., 2004, vol. 2: Kinetics and Mechanisms.
39 L. J. Richter, D. M. DeLongchamp and A. Amassian, *Chem. Rev.*, 2017, **117**, 6332–6366.
40 D. Neher, *Macromol. Rapid Commun.*, 2001, **22**, 1365–1385.
41 U. Scherf and E. J. W. List, *Adv. Mater.*, 2002, **14**, 477–487.
42 T. Miteva, A. Meisel, W. Knoll, H. G. Nothofer, U. Scherf, D. C. Müller, K. Meerholz, A. Yasuda and D. Neher, *Adv. Mater.*, 2001, **13**, 565–570.
43 W. C. Tsoi and D. G. Lidzey, *J. Phys. Condens. Matter*, 2008, **20**, 125213.
44 M. G. Munowitz, R. G. Griffin, G. Bodenhausen and T. H. Huang, *J. Am. Chem. Soc.*, 1981, **103**, 2529–2533.
45 E. R. deAzevedo, W.-G. Hu, T. J. Bonagamba and K. Schmidt-Rohr, *J. Am. Chem. Soc.*, 1999, **121**, 8411–8412.
46 O. D. Bernardinelli, G. C. Faria, L. A. de Oliveira Nunes, R. M. Faria, E. R. deAzevedo and M. F. S. Pinto, *J. Phys. Chem. A*, 2012, **116**, 4285–4295.
47 E. O. Stejskal, J. Schaefer and J. S. Waugh, *J. Magn. Reson.*, 1977, **28**, 105.
48 D. Sebastiani, *ChemPhysChem*, 2006, **7**, 164–175.
49 K. Suzuki, S. Kubo, F. Aussenac, F. Engelke, T. Fukushima and H. Kaji, *Angew. Chem. Int. Ed.*, 2017, **56**, 14842–14846.
50 P. L. Burn, A. B. Holmes, A. Kraft, D. D. C. Bradley, A. R. Brown, R. H. Friend and R. W. Gymer, *Nature*, 1992, **356**, 47–49.
51 F. C. Grozema, L. P. Candeias, M. Swart, P. T. van Duijnen, J. Wildeman, G. Hadziioanou, L. D. A. Siebbeles and J. M. Warman, *J. Chem. Phys.*, 2002, **117**, 11366–11378.
52 E. R. deAzevedo, R. W. A. Franco, A. Marletta, R. M. Faria and T. J. Bonagamba, *J. Chem. Phys.*, 2003, **119**, 2923–2934.
53 A. C. Bloise, E. R. deAzevedo, R. F. Cossiello, R. F. Bianchi, D. T. Balogh, R. M. Faria, T. D. Z. Atvars and T. J. Bonagamba, *Phys. Rev. B*, 2005, **71**, 174202.
54 R. Noriega, J. Rivnay, K. Vandewal, F. P. V. Koch, N. Stingelin, P. Smith, M. F. Toney and A. Salleo, *Nat. Mater.*, 2013, **12**, 1038–1044.

55 K. Yazawa, Y. Inoue, T. Yamamoto and N. Asakawa, *Phys. Rev. B*, 2006, **74**, 094204.
56 B. Wunderlich and J. Grebowicz, in *Liquid Crystal Polymers II/III*, ed. N. A. Platé, Springer Berlin Heidelberg, 1984, pp. 1–59.
57 B. Wunderlich, M. Möller, J. Grebowicz and H. Baur, Eds., in *Conformational Motion and Disorder in Low and High Molecular Mass Crystals*, Springer Berlin Heidelberg, 1988, pp. 1–7.
58 K. Yazawa, Y. Inoue, T. Shimizu, M. Tansho and N. Asakawa, *J. Phys. Chem. B*, 2010, **114**, 1241–1248.
59 O. F. Pascui, R. Lohwasser, M. Sommer, M. Thelakkat, T. Thurn-Albrecht and K. Saalwächter, *Macromolecules*, 2010, **43**, 9401–9410.
60 D. Dudenko, A. Kiersnowski, J. Shu, W. Pisula, D. Sebastiani, H. W. Spiess and M. R. Hansen, *Angew. Chem. Int. Ed.*, 2012, **51**, 11068–11072.
61 Bohle Anne, Dudenko Dmytro, Koenen Nils, Sebastiani Daniel, Allard Sybille, Scherf Ullrich, Spiess Hans Wolfgang and Hansen Michael Ryan, *Macromol. Chem. Phys.*, 2017, **219**, 1700266.
62 R. C. Nieuwendaal, C. R. Snyder and D. M. DeLongchamp, *ACS Macro Lett.*, 2014, **3**, 130–135.
63 C. R. Snyder, R. C. Nieuwendaal, D. M. DeLongchamp, C. K. Luscombe, P. Sista and S. D. Boyd, *Macromolecules*, 2014, **47**, 3942–3950.
64 R. C. Nieuwendaal, *Magn. Reson. Chem.*, 2016, **54**, 740–747.
65 X. Shen, W. Hu and T. P. Russell, *Macromolecules*, 2016, **49**, 4501–4509.
66 Y. Yuan, J. Shu, K. Kolman, A. Kiersnowski, C. Bubeck, J. Zhang and M. R. Hansen, *Macromolecules*, 2016, **49**, 9493–9506.
67 T. Zhang, Y. Yuan, X. Cui, H. Yin, J. Gu, H. Huang and J. Shu, *J. Polym. Sci. Part B Polym. Phys.*, 2018, **56**, 751–761.
68 A. Melnyk, M. J. N. Junk, M. D. McGehee, B. F. Chmelka, M. R. Hansen and D. Andrienko, *J. Phys. Chem. Lett.*, 2017, **8**, 4155–4160.
69 D. M. DeLongchamp, R. J. Kline, Y. Jung, E. K. Lin, D. A. Fischer, D. J. Gundlach, S. K. Cotts, A. J. Moad, L. J. Richter, M. F. Toney, M. Heeney and I. McCulloch, *Macromolecules*, 2008, **41**, 5709–5715.
70 Y. Li, *Acc. Chem. Res.*, 2012, **45**, 723–733.
71 J.-S. Wu, S.-W. Cheng, Y.-J. Cheng and C.-S. Hsu, *Chem. Soc. Rev.*, 2015, **44**, 1113–1154.
72 K. Müllen and W. Pisula, *J. Am. Chem. Soc.*, 2015, **137**, 9503–9505.
73 G. C. Faria, E. R. deAzevedo and H. von Seggern, *Macromolecules*, 2013, **46**, 7865–7873.
74 T. Gullion and J. Schaefer, *J. Magn. Reson. 1969*, 1989, **81**, 196–200.
75 R. Stalder, S. R. Puniredd, M. R. Hansen, U. Koldemir, C. Grand, W. Zajaczkowski, K. Müllen, W. Pisula and J. R. Reynolds, *Chem. Mater.*, 2016, **28**, 1286–1297.
76 K. R. Graham, C. Cabanetos, J. P. Jahnke, M. N. Idso, A. El Labban, G. O. Ngongang Ndjawa, T. Heumueller, K. Vandewal, A. Salleo, B. F. Chmelka, A. Amassian, P. M. Beaujuge and M. D. McGehee, *J. Am. Chem. Soc.*, 2014, **136**, 9608–9618.
77 L. M. Ryan, R. E. Taylor, A. J. Paff and B. C. Gerstein, *J. Chem. Phys.*, 1980, **72**, 508–515.
78 M. Lee and W. I. Goldburg, *Phys. Rev.*, 1965, **140**, A1261–A1271.
79 E. Vinogradov, P. K. Madhu and S. Vega, *Chem. Phys. Lett.*, 1999, **314**, 443–450.
80 H. N. Tsao, D. M. Cho, I. Park, M. R. Hansen, A. Mavrinskiy, D. Y. Yoon, R. Graf, W. Pisula, H. W. Spiess and K. Müllen, *J. Am. Chem. Soc.*, 2011, **133**, 2605–2612.

81 K. Do, Q. Saleem, M. K. Ravva, F. Cruciani, Z. Kan, J. Wolf, M. R. Hansen, P. M. Beaujuge and J.-L. Brédas, *Adv. Mater.*, 2016, **28**, 8197–8205.
82 K. Wang, R.-Z. Liang, J. Wolf, Q. Saleem, M. Babics, P. Wucher, M. Abdelsamie, A. Amassian, M. R. Hansen and P. M. Beaujuge, *Adv. Funct. Mater.*, 2016, **26**, 7103–7114.
83 S. R. Chaudhari, J. M. Griffin, K. Broch, A. Lesage, V. Lemaur, D. Dudenko, Y. Olivier, H. Sirringhaus, L. Emsley and C. P. Grey, *Chem. Sci.*, 2017, **8**, 3126–3136.
84 C. K. Lo, B. R. Gautam, P. Selter, Z. Zheng, S. D. Oosterhout, I. Constantinou, R. Knitsch, R. M. W. Wolfe, X. Yi, J.-L. Brédas, F. So, M. F. Toney, V. Coropceanu, M. R. Hansen, K. Gundogdu and J. R. Reynolds, *Chem. Mater.*, 2018, **30**, 2995–3009.
85 C. J. Brabec, N. S. Sariciftci and J. C. Hummelen, *Adv. Funct. Mater.*, 2001, **11**, 15–26.
86 G. Dennler, M. C. Scharber and C. J. Brabec, *Adv. Mater.*, 2009, **21**, 1323–1338.
87 D. R. Kozub, K. Vakhshouri, L. M. Orme, C. Wang, A. Hexemer and E. D. Gomez, *Macromolecules*, 2011, **44**, 5722–5726.
88 L. Ye, B. A. Collins, X. Jiao, J. Zhao, H. Yan and H. Ade, *Adv. Energy Mater.*, 2018, **8**, 1703058.
89 R. C. Nieuwendaal, C. R. Snyder, R. J. Kline, E. K. Lin, D. L. VanderHart and D. M. DeLongchamp, *Chem. Mater.*, 2010, **22**, 2930–2936.
90 R. C. Nieuwendaal, H. W. Ro, D. S. Germack, R. J. Kline, M. F. Toney, C. K. Chan, A. Agrawal, D. Gundlach, D. L. VanderHart and D. M. Delongchamp, *Adv. Funct. Mater.*, 2012, **22**, 1255–1266.
91 R. Mens, S. Bertho, S. Chambon, J. D'Haen, L. Lutsen, J. Manca, J. Gelan, D. Vanderzande and P. Adriaensens, *J. Polym. Sci. Part Polym. Chem.*, 2011, **49**, 1699–1707.
92 R. Mens, F. Demir, G. V. Assche, B. V. Mele, D. Vanderzande and P. Adriaensens, *J. Polym. Sci. Part Polym. Chem.*, 2012, **50**, 1037–1041.
93 F. Etzold, I. A. Howard, N. Forler, A. Melnyk, D. Andrienko, M. R. Hansen and F. Laquai‡, *Energy Environ. Sci.*, 2015, **8**, 1511–1522.
94 R. C. Nieuwendaal, D. M. DeLongchamp, L. J. Richter, C. R. Snyder, R. L. Jones, S. Engmann, A. Herzing, M. Heeney, Z. Fei, A. B. Sieval and J. C. Hummelen, *Phys. Rev. Lett.*, 2018, **121**, 026101.